4

Solid State Research

1968

Prepared under Electronic Systems Division Contract AF 19(628)-5167 by

Lincoln Laboratory

MASSACHUSETTS INSTITUTE OF TECHNOLOGY

Lexington, Massachusetts

The work reported in this document was performed at Lincoln Laboratory, a center for research operated by Massachusetts Institute of Technology, with the support of the U.S. Air Force under Contract AF 19(628)-5167.

4

Solid State Research

1968

Issued 27 December 1968

Lincoln Laboratory

MASSACHUSETTS INSTITUTE OF TECHNOLOGY

Lexington, Massachusetts

ABSTRACT

This report covers in detail the solid state research work at Lincoln Laboratory for the period 1 August through 31 October 1968. The topics covered are Solid State Device Research, Optical Techniques and Devices, Materials Research, and Physics of Solids.

Accepted for the Air Force
Franklin C. Hudson
Chief, Lincoln Laboratory Office

INTRODUCTION

I. SOLID STATE DEVICE RESEARCH

Experiments with the fast far-infrared and submillimeter germanium impact ionization modulator have been extended to p-type Ge samples and additional wavelengths. Much improved depth of modulation has been obtained at all wavelengths investigated and very nearly 100-percent modulation has been achieved for 2-mm wavelength radiation.

In a communications-type experiment, 337-μ cyanide laser radiation was modulated by applying an audio modulated 300-kHz carrier to the Ge modulator. This radiation was incident on a fast GaAs photoconductive detector which was connected to a radio receiver tuned to 300 kHz, where the audio information was recovered.

Gallium-tin melts have been used in the $AsCl_3$-Ga-H_2 flow system to prepare n-type epitaxial GaAs with accurately controlled, uniform electron carrier densities in the range between 10^{15} and 10^{17} cm^{-3}. The transfer ratio of net tin donor concentration in the epitaxial layer to tin concentration in the gallium melt was examined as a function of seed orientation, seed and melt temperatures, and flow rates. Over a wide range of conditions, the tin transfer ratio depends primarily on the growth rate of the epitaxial layer. Doping variations as low as ± 2.6 percent have been attained by growing under conditions where system variations have little effect on growth rate.

Infrared transmission, magnetic birefringence, and Faraday rotation have been measured in single crystals of EuO in the wavelength range between 1.5 and 20 μ. The most transparent samples have an absorption coefficient at 20°K less than 0.5 cm^{-1} in the range between 2.5 and 9 μ, and less than 1.0 cm^{-1} at 10.6 μ. At 20°K and 9 kG, the Faraday rotation varies from 660 deg/cm at 10.6 μ to 3×10^4 deg/cm at 2.5 μ, and over 10^5 deg/cm at 1.5 μ. This corresponds to a figure of merit for the specific rotation per unit attenuation of 150 deg/dB at 10.6 μ and $>1.4 \times 10^4$ deg/dB at 2.5 μ.

II. OPTICAL TECHNIQUES AND DEVICES

Frequency response measurements of two Ge:Cu detectors have been performed by the optical heterodyne technique involving a tunable diode laser.

A stable reference laser has been heterodyned with the CO_2 laser amplifier output and the beat frequency spectra observed with both sealed-off and flowing-gas operation of the amplifier. These measurements showed no significant deterioration of the beat frequency spectrum in sealed-off operation; however, with flowing-gas operation of the amplifier, the envelope of the beat frequency spectrum broadened by about an order of magnitude from 5 to 50 kHz for 1-sec observation time.

Stability measurements have indicated that the expected improvements in short-term stability will be achieved in the redesigned version of the stable laser, in addition to the significantly improved ease of assembly, operation, and reduced cost.

Preliminary analysis indicates that it is feasible to measure the spatial correlation of random phase fluctuations of 10-μ radiation propagating in the atmosphere by using a tracking telescope.

Experiments have been carried out to determine the effects of molecular diffusion on the saturation parameter of the CO_2 laser. The equivalent saturation parameter derived from these measurements decreased monotonically from 97 to 35 W/cm^2 as the average input beam radius increased from 0.87 to 2.47 mm in the 9-mm radius discharge tube of the amplifier.

The transmission of the atmosphere for the P(18) and P(22) lines of a CO_2 laser has been measured over a 1.3-km path for partial pressures of H_2O vapor ranging from 10 to 25 mb.

An expression has been derived for the optical heterodyne mixing efficiency as a function of detector position with respect to the focus. The efficiency has been evaluated in a number of important cases.

III. MATERIALS RESEARCH

A numerical scale for the oxygen affinity of metals has been constructed by arranging the metals in order of their "pO" values, where pO is defined as the negative logarithm of the oxygen pressure (in atmospheres) in equilibrium with the metal and its lowest oxide at 1000°K. In general, the oxygen affinity increases as pO increases, since in most cases pO is proportional to the free energy of the reaction in which the metal combines with one mole of oxygen to form the lowest oxide.

The liquidus surface in the Zn-Cd-Te ternary system has been investigated by means of differential thermal analysis. Most of the liquidus temperature measurements were made on samples containing between 50 and 100 atomic-percent Te.

A system has been constructed for making differential thermal analysis measurements from 400°K down to about 15°K. It has been used successfully to detect the thermal effects accompanying the magnetic transition in CoS_2 at 124°K and the cubic-rhombohedral transformation in $Sn_{0.8}Ge_{0.2}Te$ alloy at 180°K.

Single crystals of $Eu_{3-x}Gd_xFe_5O_{12}$ garnets up to 22 mm on a side have been grown from a $PbO-PbF_2-B_2O_3$ flux. Smaller crystals of $Eu_3Fe_5O_{12}$ have been grown from Fe_2O_3 and $BaFe_{12}O_{19}$ fluxes, which are being used in an attempt to reduce contamination of the garnet crystals.

A new series of rare-earth compounds, with the type formula $LnCrTeO_6$, has been prepared by reacting mixtures of the metal oxides at 1000°C. These compounds have

a structure similar to that of $PbSb_2O_6$, but ordering of Cr and Te to form Cr^{3+}-Te^{6+}-Cr^{3+} columns causes a doubling of the c-parameter.

The phase diagram of $CsNiF_3$ has been determined by means of x-ray diffraction measurements on samples annealed at pressures up to 65 kbars and temperatures between 500° and 1000°C. The hexagonal two-layer structure stable at atmospheric pressure is transformed at less than 5 kbars to a hexagonal nine-layer structure which, in turn, is transformed at about 50 kbars to the hexagonal six-layer structure reported previously.

Further studies have been made on the structural, electrical, and magnetic properties of the high-pressure form of $CdCr_2Se_4$ reported previously. This phase exhibits antiferromagnetic ordering with a Néel temperature of 55°K, whereas the phase stable at atmospheric pressure is ferromagnetic.

IV. PHYSICS OF SOLIDS

The oscillatory magnetoreflection data of bismuth-antimony alloys in the range of composition $0 < \%Sb < 15$ have been analyzed in terms of the Lax two-band model. The variation of the band parameters with composition can be understood qualitatively in terms of the change in magnitude of the spin-orbit splitting with alloying.

The Shubnikov-de Haas effect is being used to investigate the Fermi surface of PbTe-SnTe alloys. Measurements have been carried out in 17-, 20-, and 30-percent tin alloys in the temperature range 1.25° to 4.2°K with magnetic fields up to 80 kG.

The problem of transport in an impure normal Fermi system has been studied. A quasi-particle transport equation has been derived for this system subject to the limitations of low temperatures, small impurity densities, and slowly varying driving fields.

A study has been made of what information can be obtained about the symmetry of the ground state of a system from general considerations. On the basis of a general relation between nodelessness and symmetry of a wavefunction, it is found that the symmetry of the ground level can be predicted for many systems of physical interest.

Recently, it was shown that five distinct distant-neighbor B-B exchange interactions can play significant roles in determining the ground state spin configuration in chromium spinels having nonmagnetic A-site ions. Extension of this work to the case of magnetic A-site ions and including A-A interactions has led, in cobalt chromite, to (a) an 8-percent decrease in the theoretical wavelength of the ferrimagnetic spiral, and (b) the prediction of an additional magnetic transition at a temperature of about one-third of T_c. These new results bring the theory into overall agreement with experiment.

A new generalization of Hartree-Fock (HF) theory to nonzero temperature, namely, the Thermal Single-Determinant Approximation, has been applied (a) to a homogeneous

interacting electron gas, with the result that a plane wave solution is found with identical thermodynamic behavior to that of the standard thermal HF approximation (STHFA), and (b) to H-atoms, where the new theory gives a lower free energy than the STHFA. Furthermore, the new theory requires that for weakly interacting atoms the one-electron functions ψ_i be localized, whereas the STHFA requires that the ψ_i be extended throughout the crystal.

The fact that the statistical mechanics of the Heisenberg Hamiltonian for infinite-dimensional spin and the exactly soluble spherical model are identical has been used to obtain some useful results. The high-temperature expansions are found to agree well with the exact calculations, and a conjectured form of the free energy for the model in a three-dimensional lattice is obtained.

The temperature dependences in α-quartz of the damping of two optic vibrations, the 128-cm^{-1} E-mode and the 466-cm^{-1} A_1-mode, and a longitudinal acoustic vibration along the x-axis have been measured by high-resolution Raman and Brillouin scattering. A simple model for the cubic anharmonicity, which includes relaxation broadening of the thermal phonons, accounts satisfactorily for the damping of these modes.

Scattering of light from magnetic excitations in $RbNiF_3$ has been observed below T_c (139°K) and up to ~200°K. The Raman scattering observations give exchange constants which are consistent with magnon-assisted optical absorption and high-temperature susceptibility data.

By use of an argon-ion laser and a surface reflection technique, Raman scattering from zone center optic phonons has been studied in InSb and InAs from 5° to 300°K. In both these semiconductors, an enhancement of the LO phonon scattering intensity takes place when the laser frequency is near an interband transition. LO phonon scattering enhancement and also a decrease in the LO scattering frequency are obtained when an InAs surface is biased with an electric field. The latter InAs results are explained in terms of the change in dielectric constant with surface electric field.

The effect of spin-density fluctuations on the scattering from single-particle excitations in GaAs has been studied. Because charge-density fluctuations are screened out in high-electron concentration materials, while spin-density fluctuations are not, the spin-density fluctuations play an important role in this case. The polarization properties of the two mechanisms are also found to be different.

Careful evaluation of two single-electron mechanisms proposed to explain the magneto-Raman process with $\Delta n = 1$, $\Delta s = 0$ in InSb (namely, interactions (a) due to the linear k, inversion asymmetry terms in the E(k) of the valence band, and (b) between Landau levels which occur with $k_3 \neq 0$, where k_3 is along the magnetic field) gives a cross section several orders of magnitude smaller than experimental results. This suggests that other mechanisms, such as Coulomb interactions, are important. Objections are raised to previous theoretical estimates of this cross section.

CONTENTS

ORGANIZATION

SOLID STATE DIVISION

A. L. McWhorter, *Head*
P. E. Tannenwald, *Associate Head*
M. J. Hudson, *Assistant*
E. P. Warekois

SOLID STATE THEORY

H. J. Zeiger, *Leader*
M. M. Litvak, *Assistant Leader*

Argyres, P. N.
Brine, N. S.
Chinn, S. R.*
Dresselhaus, G. F.
Hamilton, D. C.
Hanus, J.
Kaplan, T. A.
Kelley, P. L.
Kleiner, W. H.
Landon, S. N.
Larsen, D. M.
Palm, B. J.†
Sigel, J. L.
Stanley, H. E.

OPTICS AND INFRARED

R. H. Kingston, *Leader*
R. J. Keyes, *Assistant Leader*

Bates, D. H.
Bostick, H. A.
Carbone, R. J.
Freed, C.
Gilmartin, T. J.
Hinkley, E. D.
Longaker, P. R.
McPhie, J. M.
O'Donnell, R. G.
Quist, T. M.
Ross, A. H. M.
Sullivan, F. M.
Swezey, L.
Zimmerman, M. D.

ELECTRONIC MATERIALS

J. B. Goodenough, *Leader*
A. J. Strauss, *Associate Leader*

Anderson, C. H., Jr.
Andrews, H. I.*
Arnott, R. J.
Banus, M. D.
Batson, D. A.
Brebrick, R. F., Jr.
Button, M. J.
Capes, R. N.
Delaney, E. J.
England, R. E.
Fahey, R. E.
Ferretti, A.
Finn, M. C.
Hilton, T. W.
Iseler, G. W.
Kafalas, J. A.
Kasper, H. M.
LaFleur, W. J.
Lavine, M. C.†
Longo, J. M.
Mastromattei, E. L.
O'Connor, J. R.
Owens, E. B.
Plonko, M. C.
Raccah, P. M.
Reed, T. B.
Roddy, J. T.
Searles, I. H.
Smith, F. T. J.
Steininger, J. A.
Whentley, G. E.

SOLID STATE PHYSICS

J. G. Mavroides, *Leader*
G. B. Wright, *Assistant Leader*

Blum, F. A.
Brandt, R. C.
Burke, J. W.
Crooker, P. P.
Dresselhaus, M. S.†
Dwight, K., Jr.
Feinleib, J.
Feldman, B.
Fulton, M. J.
Groves, S. H.
Henrich, V. E.
Johnson, E. J.
Kernan, W. C.
Kolesar, D. F.
Krag, W. E.
Melngailis, J.
Menyuk, N.
Nill, K. W.
Parker, C. D.
Perry, F. H.
Pine, A. S.
Scouler, W. J.
Strahm, N. D.*
Tichovolsky, E. J.*
Waldman, J.*
Weber, R.

APPLIED PHYSICS

J. O. Dimmock, *Leader*
T. C. Harman, *Assistant Leader*
I. Melngailis, *Assistant Leader*

Brueck, S.*
Butler, J. F.
Calawa, A. R.
Carter, F. B.
Caswell, F. H.
Clough, T. F.
Donaldson, P. L.
Donnelly, J. P.
Ferrante, G.
Foyt, A. G.
Hurwitz, C. E.
Lindley, W. T.
Mooradian, A.
Murphy, R. A.*
Oliver, M. R.*
Orphanos, W. G.*
Paladino, A. E.
Phelan, R. J., Jr.
Stillman, G. E.
Ward, J. H. R., III
Wolfe, C. M.
Youtz, P.

---

* Research Assistant

† Part Time

REPORTS BY AUTHORS ENGAGED IN SOLID STATE RESEARCH

15 August through 15 November 1968

PUBLISHED REPORTS

Journal Articles*

JA No.			
3048	Performance Characteristics of Thermomagnetic Devices Involving Graded Mass and Gap. I. Generators	J. M. Honig B. Lax	J. Appl. Phys. 39, 3549 (1968)
3195	Electrical Properties of Ti_2O_3 Single Crystals	J. M. Honig T. B. Reed	Phys. Rev. 174, 1020 (1968)
3206	Partial Pressure of $Se_2(g)$ in Selenium Vapor	R. F. Brebrick	J. Chem. Phys. 48, 5741 (1968)
3219	Tuning of PbSe Lasers by Hydrostatic Pressure from 8 to 22 μ	J. M. Besson† W. Paul† A. R. Calawa	Phys. Rev. 173, 699 (1968)
3223	Upper and Lower Bounds for the Intermediate-Coupling Polaron Ground-State Energy	D. M. Larsen	Phys. Rev. 172, 967 (1968)
3255	Intermediate-Coupling Polaron Effective Mass	D. M. Larsen	Phys. Rev. 174, 1046 (1968)
3273	Optical Heterodyne Detection at 10.6 μm of the Beat Frequency Between a Tunable $Pb_{0.88}Sn_{0.12}Te$ Diode Laser and a CO_2 Gas Laser	E. D. Hinkley T. C. Harman C. Freed	Appl. Phys. Letters 13, 49 (1968)
3276	Far-Infrared Photoconductivity in High-Purity Epitaxial GaAs	G. E. Stillman C. M. Wolfe I. Melngailis C. D. Parker P. E. Tannenwald J. O. Dimmock	Appl. Phys. Letters 13, 83 (1968)
3280	Pressure-Induced Structural Changes in the System $Ba_{1-x}Sr_xRuO_3$	J. M. Longo J. A. Kafalas	Materials Res. Bull. 3, 687 (1968), DDC 674791
3303	Quenchable Effects of High Pressures and Temperatures on the Cubic Monoxide of Titanium	M. D. Banus	Materials Res. Bull. 3, 723 (1968)

* Reprints available.

† Author not at Lincoln Laboratory.

Reports

JA No.			
3306	Band Structure and Electrical Conductivity of NiO	J. Feinleib D. Adler*	Phys. Rev. Letters 21, 1010 (1968)
3316	Preparation of $\{A_3^{2+}\}$ $[Te_2]$ (B_3^{2+})-Garnets	H. M. Kasper	Materials Res. Bull. 3, 765 (1968)
MS-2249	Ultraviolet and Infrared Pumping of OH Molecules	M. M. Litvak	Interstellar Ionized Hydrogen, Y. Terzian, ed. (W. A. Benjamin Inc., New York, 1968)

* * * * *

UNPUBLISHED REPORTS

Journal Articles

JA No.			
3082	Symmetry of the Ground Level of a Hamiltonian	W. H. Kleiner T. A. Kaplan	Accepted by J. Math. Phys.
3264	Magneto-Optical Properties	J. G. Mavroides	Accepted as a chapter in Optical Properties of Solids, F. Abeles, ed. (North-Holland, Amsterdam)
3267	Spherical Model as the Limit of Infinite Spin Dimensionality	H. E. Stanley	Accepted by Phys. Rev.
3286	Homogeneity Ranges and Te_2-Pressure Along the Three-Phase Curves for Bi_2Te_3(c) and a 55-58 at % Te, Peritectic Phase	R. F. Brebrick	Accepted by J. Phys. Chem. Solids
3295	Low Level Coherent and Incoherent Detection in the Infrared	R. J. Keyes T. M. Quist	Accepted as a chapter in Semiconductors and Semimetals, Vol. VII
3300	Metallic Inclusions and Cellular Substructure in $Pb_{1-x}Sn_xTe$ Single Crystals	J. F. Butler T. C. Harman	Accepted by J. Electrochem. Soc.
3311	Effect of Pressure on the Magnetic Properties of MnAs	N. Menyuk J. A. Kafalas K. Dwight J. B. Goodenough	Accepted by Phys. Rev.
3312	Effect of the Molecular Interaction on the AC Kerr Effect: Possibility of a Field-Induced Phase Transition	J. Hanus	Accepted by Phys. Rev.

* Author not at Lincoln Laboratory.

JA No.			
3313	Exact Solution for a Linear Chain of Isotropically Interacting Classical Spins of Arbitrary Dimensionality	H. E. Stanley	Accepted by Phys. Rev.
3326	Characterization of Phases in the 50-60 at % Te Region of the Bi-Te System by X-Ray Powder Diffraction Patterns	R. F. Brebrick	Accepted by J. Appl. Crystal.
3329	Isolation of Junction Devices in GaAs Using Proton Bombardment	A. G. Foyt W. T. Lindley C. M. Wolfe J. P. Donnelly	Accepted by Solid State Electron.
3336	Epitaxially Grown Guard Rings for GaAs Diodes	C. M. Wolfe W. T. Lindley	Accepted by J. Electrochem. Soc.
3345	Optical Properties of Mg_2Si, Mg_2Ge and Mg_2Sn from 0.6 to 11.0 eV at 77°K	W. J. Scouler	Accepted by Phys. Rev.
3348	Temperature Dependence of Raman Linewidth and Shift in α-Quartz	A. S. Pine P. E. Tannenwald	Accepted by Phys. Rev.
3350	The P-T Phase Diagram of InSb at High Temperatures and Pressures	M. D. Banus M. C. Lavine	Accepted by J. Appl. Phys.
3353	$LnCrTeO_6$ – A New Series of Compounds Based on the $PbSb_2O_6$ Structure	H. M. Kasper	Accepted by Materials Res. Bull.
3371	Bismuth Doped $Pb_{1-x}Sn_xTe$ Diode Lasers with Low Threshold Currents	J. F. Butler T. C. Harman	Accepted by IEEE J. Quant. Electron.

Meeting Speeches*

MS No.			
1908B	Modern High Pressure Techniques	J. A. Kafalas	High Pressure Treatment of Materials Meeting, Boston, 7 November 1968
2015B	Survey of Equipment for High Pressure Studies	M. D. Banus	
2016B	Retained High Pressure Phases and High Pressure Synthesis	M. D. Banus	
1954C	Localized vs Collective Descriptions of Magnetic Electrons	J. B. Goodenough	American Chemical Society, Atlantic City, New Jersey, 8-13 September 1968

* Titles of Meeting Speeches are listed for information only. No copies are available for distribution.

Reports

MS No.			
2327	$SrIrO_3$ – A Study of the High and Low Pressure Forms	J. M. Longo J. A. Kafalas	American Chemical Society, Atlantic City, New Jersey, 8-13 September 1968
2328	The P-T Phase Diagram of InSb at High Temperatures and Pressures	M. D. Banus M. C. Lavine	
1954D	A Phase Diagram for Outer Electrons in Solids	J. B. Goodenough	Colloquium, Johns Hopkins University, 15 October 1968
2112A	High Temperature Techniques for Material Preparation and Crystal Growth	T. B. Reed	Argonne National Laboratory, Argonne, Illinois, 27 September 1968
2236A	Raman Scattering from Magneto-plasma Waves in Semiconductors	A. L. McWhorter P. N. Argyres	International Conference on Light Scattering Spectra of Solids, New York University, 3-6 September 1968
2325	Thermal Brillouin Scattering Study of the Attenuation of Hypersound in Quartz	A. S. Pine	
2331	Raman Scattering from Electron Spin-Density Fluctuations in GaAs	D. C. Hamilton A. L. McWhorter	
2332	Light Scattering from Single Particle Electron and Hole Excitations in Semiconductors	A. Mooradian	
2333	Raman Scattering from Lattice Vibrations of $GaAs_xP_{1-x}$	N. D. Strahm A. L. McWhorter	
2334	Landau Level Raman Scattering	G. B. Wright P. L. Kelley S. H. Groves	
2335	Light Scattering from Plasmons and Phonons in GaAs	A. Mooradian A. L. McWhorter	
2251A	Homogeneity Ranges and Te_2-Pressure Along the Three-Phase Curves for Bi_2Te_3(c) and a 55-58 at % Te, Peritectic Phase	R. F. Brebrick	American Chemical Society, Boston, 13-15 October 1968
2361	Polymorphism in Selenospinels – A High Pressure Phase of $CdCr_2Se_4$	M. D. Banus M. C. Lavine	
2362	The High-Pressure Form of $CsNiF_3$ – A Transparent Ferrimagnet	J. M. Longo J. A. Kafalas	
2363	Thermal Arrests in the Bi-Te System	A. J. Strauss	

MS No.			
2261B	Band Approach to the Transition Metal Oxides	J. Feinleib	Seminar, Sandia Laboratory, Albuquerque, New Mexico, 25-27 September 1968
2316	A Phase Diagram for Electrons in Solids	J. B. Goodenough	Seminar, University of Texas, 13 November 1968
2330	Dependence of Critical Properties on Dimensionality of Spins	H. E. Stanley	International Conference on Statistical Mechanics, Kyoto, Japan, 9-14 September 1968
2332A, B, C, D	Light Scattering from Elementary Excitations in Solids Using Intense Laser Sources	A. Mooradian	Seminar, Ohio State University, 15 October 1968; Seminar, Purdue University, 19 October 1968; Seminar, Yale University, 22 October 1968; Seminar, M. I. T. National Magnet Laboratory, 24 September 1968
2340	Tin Doping of Epitaxial Gallium Arsenide	C. M. Wolfe G. E. Stillman W. T. Lindley	International Conference on Gallium Arsenide, Dallas, Texas, 16-18 October 1968
2359	Far Infrared Impact Ionization Modulators	I. Melngailis P. E. Tannenwald	NEREM, Boston, 6-8 November 1968
2386	Self-Modulation, Self-Steepening and Spectral Development of Light in Small Scale Trapped Filaments	T. K. Gustafson* J-P. Taran* H. A. Haus* J. R. Lifsitz* P. L. Kelley	Gordon Conference, Meriden, New Hampshire, 24-30 August 1968
2392	Self-Trapping of a CW Laser Beam in Glasses	R. L. Carman A. Mooradian P. L. Kelley	
2410	Properties of Insulating Regions in GaAs Created by Proton Bombardment	W. T. Lindley A. G. Foyt J. P. Donnelly C. M. Wolfe	Electrochemical Society, Montreal, Canada, 6-11 October 1968
2411	Interdiffusion in PbSe	R. W. Brodersen* J. N. Walpole* A. R. Calawa	
2420	Photon-Electron Interactions in Solids	A. Mooradian	Seminar, Purdue University, 18 October 1968
2420A, B, C	Light Scattering from Electrons in Solids	A. Mooradian	Seminar, M. I. T., 11 October 1968; Seminar, M. I. T., 8 November 1968; Seminar, IBM Research Laboratories, Yorktown Heights, New York, 14 November 1968

* Author not at Lincoln Laboratory.

Reports

MS No.			
2429	Maser Emission in Interstellar OH	M. M. Litvak	Seminar, Harvard College Observatory, 23 October 1968
2430	Light Scattering from Electrons in Semiconductors	A. L. McWhorter	Seminar, General Telephone and Electronics Laboratories, Bayside, New York, 28 October 1968

I. SOLID STATE DEVICE RESEARCH

A. FAR-INFRARED AND SUBMILLIMETER IMPACT IONIZATION MODULATOR

Experiments with the fast germanium modulator described previously[1] have been extended to p-type Ge samples and additional wavelengths. Due to the lower mobility and attendant increased free-carrier absorption in p-type Ge, much improved depth of modulation has been obtained. Table I-1 shows a summary of the results. Nearly 100-percent modulation is achieved for 2-mm wavelength radiation. An example of this is shown in Fig. I-1, where the results of mechanical modulation by means of a chopping wheel, and simultaneous electrical modulation by applying 20-μsec current pulses to the Ge modulator are displayed. During the "on" cycle of square-wave mechanical modulation, the power at the detector (InSb) is reduced to almost zero when the Ge is pulsed.

The dependence of the modulation index on current at the various wavelengths is shown in Fig. I-2 for a p-type Ge sample. The maximum modulation at each wavelength was achieved by using pulsed current in order to avoid heating of the Ge sample. To determine the maximum rms current that can be applied without causing excessive heating, both ends of a sample were soldered to individual copper heatsinks in a separate test, and the assembly was immersed in liquid helium. For the p-type Ge sample of Fig. I-1, the maximum rms current was about 0.5 A.

TABLE I-1

PROPERTIES OF Ge MODULATORS AT 4.2°K

Sample Dimensions (mm)	$\lvert N_A - N_D \rvert$ (cm^{-3})	Maximum Modulation				Saturation Current (A)
		λ = 195 μ	λ = 337 μ	λ = 0.9 mm	λ = 2.15 mm	
4 × 4 × 1.3	1.3×10^{15} (p)	0.35	0.50	0.8	0.95	1.4
4 × 4 × 1	0.95×10^{15} (p)	–	0.50	0.75	–	0.8
4 × 4 × 1	0.5×10^{15} (n)	–	~0.03	0.25	0.6	0.3
4 × 4 × 1	0.5×10^{15} (n)	–	–	0.25	–	0.3

-85-7345-1

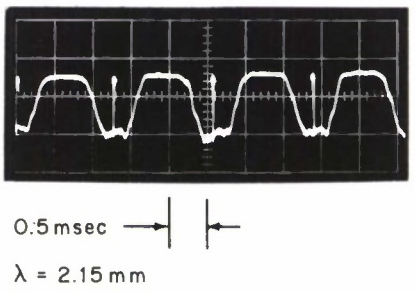

Fig. I-1. Depth of modulation produced by Ge modulator. Trace shows output of InSb detector when 2.15-mm radiation is simultaneously chopped by mechanical wheel (800 Hz) and by 2-μsec long 1.5-A pulses in Ge modulator.

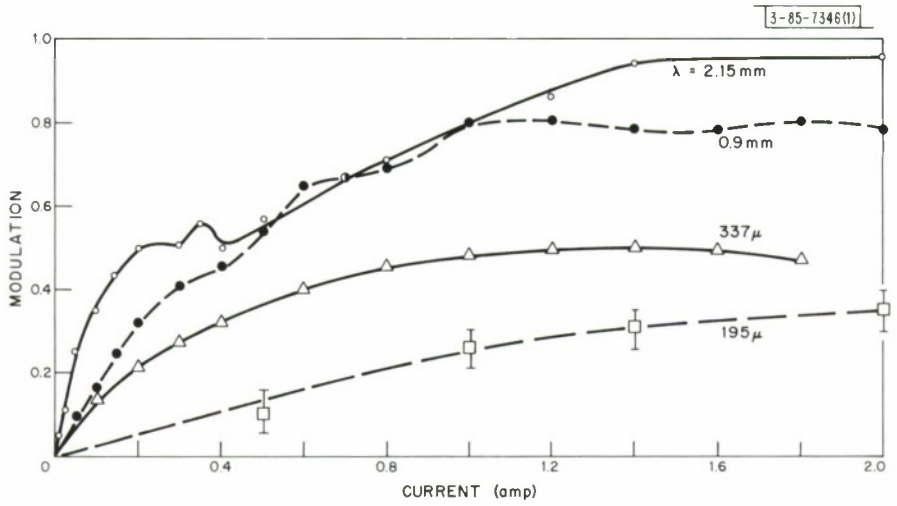

Fig. I-2. Modulation index as a function of current in 1.3-mm thick p-type Ge ($N_A - N_D = 1.3 \times 10^{15}$ cm^{-3}).

Thus, the maximum CW modulation achievable with the sample in this configuration can be determined for each of the wavelengths from Fig. I-1.

I. Melngailis
P. E. Tannenwald
C. D. Parker

B. VOICE MODULATION OF FAR-INFRARED LASER BEAM

A communications-type experiment was carried out to demonstrate one application of the far-infrared and submillimeter ionization modulator discussed in Sec. I-A above. A 300-kHz carrier of sufficient magnitude to cause impact ionization was applied to the Ge, which resulted in modulation of the 337-μ cyanide laser radiation transmitted through it. The 300-kHz carrier itself was audio modulated, and the 337-μ submillimeter radiation was then incident on a fast GaAs photoconductive detector which was connected to a radio receiver tuned to 300 kHz, where the audio information was recovered. For simplicity in this initial experiment, the modulator and detector were contained in the same low-temperature dewar such that a short section of light pipe constituted the transmission path. The audio information could have been used directly to modulate the 337-μ beam, but utilization of the 300-kHz subcarrier avoided the large low-frequency noise accompanying the laser gas discharge and at the same time demonstrated the high-frequency capability of the modulator and detector.

G. E. Stillman
I. Melngailis
C. D. Parker

C. TIN DOPING OF EPITAXIAL GALLIUM ARSENIDE

Gallium-tin melts have been used with the $AsCl_3$-Ga flow system[2,3] to prepare n-type epitaxial GaAs with carrier densities from 5×10^{15} to 2×10^{17} cm^{-3}. This range of tin doping is about a factor of five above the residual impurity level, and a factor of five below possible solubility limits. The transfer ratio of net tin donor concentration in the epitaxial layer to tin concentration in the gallium melt has been examined as a function of seed orientation, growth

rate, seed and melt temperatures, and flow rates. Over a wide range of conditions, the tin transfer ratio is dominated by its growth-rate dependence. This dominant growth-rate behavior can be qualitatively explained by a time-dependent adsorption of tin at the vapor-solid interface. Tin acceptors have the same growth-rate dependence as the tin donors, and are incorporated into the layer in the ratio of about one acceptor for every three donors. Because of the dominant growth-rate dependence, uniformly doped layers can be obtained under conditions where small variations in temperature and flow rate have little effect on the growth rate and therefore the doping. Under these conditions, average measured doping variations as low as ±2.6 percent have been attained.

Figure I-3 shows the variation of tin transfer ratio with growth rate for the four low-index planes. As shown, the transfer ratio decreases with increasing growth rate for the {111} As, {110}, and {100} surfaces up to a growth rate of about 0.15 μ/min. A solid line has been drawn through these points. Beyond this value, corresponding to the dashed line in the figure, the transfer ratio begins to increase with growth rate for the {100} and the {111} Ga surfaces, and above about 0.5 μ/min the {111} Ga growth becomes noticeably rough. Under the conditions required to obtain reasonable growth rates for the other low-index planes, the {111} Ga growth rate was high and the layers were rough. Note that, although the growth rates and the tin transfer ratios are markedly different for layers of different orientation which are grown under the same conditions, the dependence of the transfer ratio on the growth rate appears to be the same for all low-index planes.

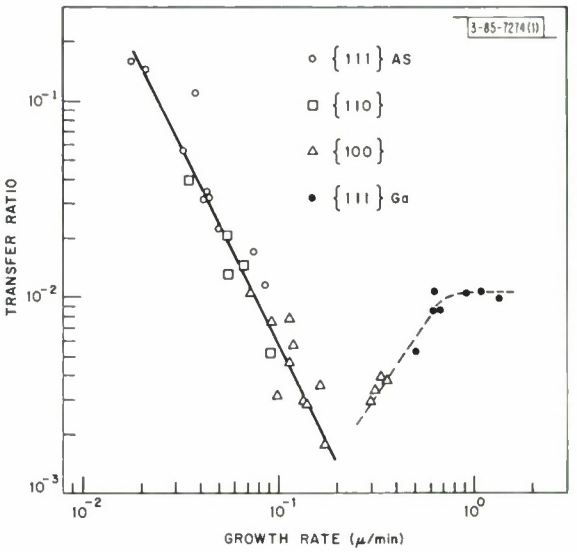

Fig. I-3. Growth rate dependence of tin transfer ratio for {111} As, {110}, {100}, and {111} Ga planes.

We believe this growth-rate behavior can be explained qualitatively in the following manner. At the lower growth rates, the incorporation of tin into the epitaxial layer is controlled by a time-dependent adsorption.† That is, the tin is readily adsorbed on the growing surface and the amount desorbed is very small. Because of this, the longer a growing surface is exposed to the flux of tin, or the slower the growth rate, the larger the amount of tin incorporated into the epitaxial layer. This behavior holds up to a growth rate so large that the crystal surface becomes nonsingular and a larger surface area per unit volume is available for adsorption. With the larger surface area for adsorption, the tin incorporated into the epitaxial layer begins to increase with growth rate and, as the growth rate increases further, the growth becomes dendritic corresponding to a noticeably rougher surface.

† Adsorption has been previously used to account for variations in impurity segregation with crystallographic orientation and growth rate by Hall[4] for melt-grown Ge and Si, by Banus and Gatos[5] for melt-grown InSb, and by Williams[6] for vapor-grown GaAs.

To determine the tin acceptor concentration, layers were doped to high enough levels to ensure that residual acceptors would have little effect on the electrical properties. At these levels, it was difficult to analyze the temperature dependence of the Hall constant because of the effects of impurity band or degenerate conduction. The tin aeeeptor concentration was therefore determined by analyzing the Hall mobility with the Brooks-Herring equation[7] for ionized impurity scattering. Since lattice seattering decreases with decreasing temperature while the amount of impurity band or degenerate conduction inereases, there exists an optimum temperature for this mobility analysis. These two competing effects produee a minimum in the compensation ratio calculated from Hall mobility and earrier conеentration data as a funetion of temperature using the Brooks-Herring equation. The minimum compensation ratio determined in this manner was used to define an upper limit on the concentration of tin aeeeptors. Results of this analysis for two orientations from the same run are shown in Table I-2. These results indieate that tin is incorporated into the growing crystal in the ratio of about one tin aeeeptor for every three tin donors, independent of growth rate and erystallographie orientation. This compensation ratio of one-to-three is probably determined by the As-to-Ga ratio in this system.

TABLE I-2
TIN ACCEPTOR CONCENTRATION

Plane	{111} As	{100}
Growth Rate (μ/min)	0.043	0.093
N_D (cm^{-3})	5.2×10^{17}	2.8×10^{16}
N_A (cm^{-3})	1.8×10^{17}	9.7×10^{15}
N_A/N_D	0.35	0.35
T (°K)	130	60

Figure I-4 shows doping variations parallel to the growth axis for three {100} layers grown under different conditions with the same degree of eontrol over the growth parameters. These profiles were obtained by differential capacitance measurements on Schottky barrier diodes. The vertical scale has been greatly enlarged to amplify small variations in the doping level. The upper profile is for a layer grown under conditions (previously determined from other data) where small perturbations of the growth parameters should result in appreciable changes in growth rate. The lower two profiles are for layers whieh were grown under conditions where the growth rate would be expected to vary little with growth parameter changes.† The upper profile has an average measured deviation of ±16.5 percent with a maximum variation of about 40 pereent. The lower profiles have average variations of ±3.4 and ±2.6 pereent, with maximum measured deviations of about 6 percent. Considering the aeeuracy of the measurement, much of the variation in

† In our system, little change in {100} growth rate is observed for gallium melt temperatures from 890° to 920°C, for growth temperatures from 700° to 740°C, for $AsCl_3$ fluxes from 2×10^{-5} to 5×10^{-5} mole/min, and for total hydrogen flows from 200 to 300 ml/min.

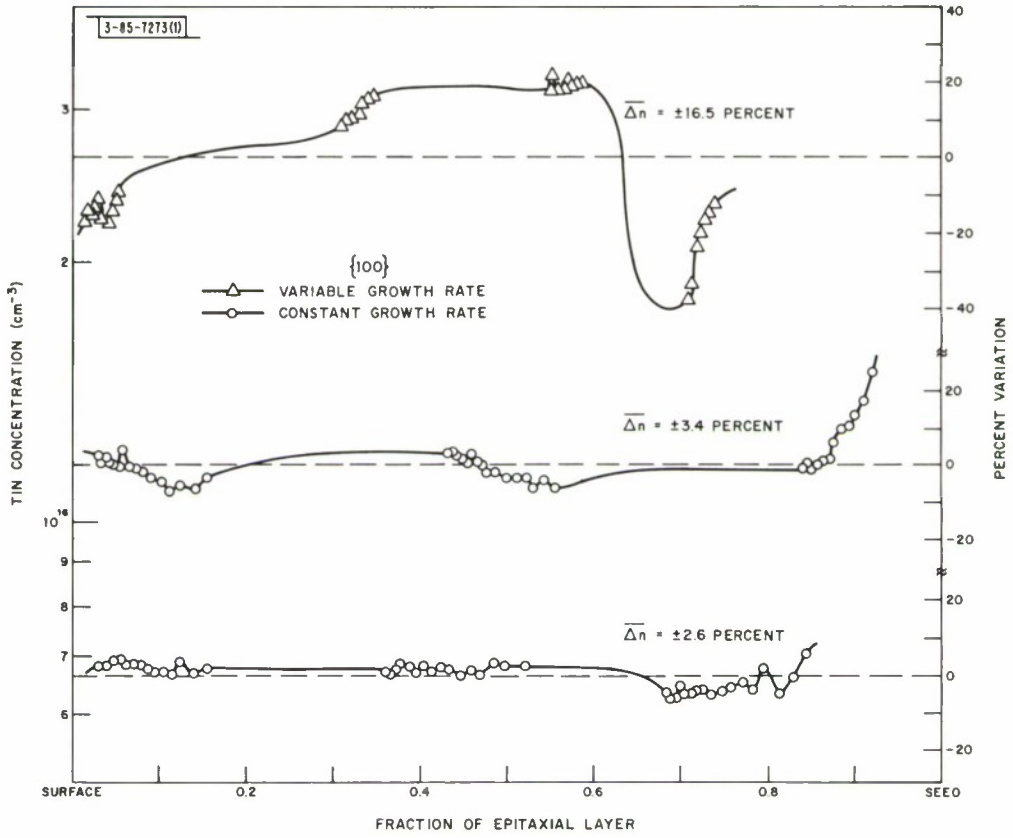

Fig. I-4. Doping variations parallel to growth axis for {100} epitaxial layers grown on low-resistance substrates. Vertical scale has been amplified to indicate small variations in doping. Upper profile corresponds to layer grown under conditions where small variations of temperature and flow will vary growth rate and thus doping; lower two profiles were grown under conditions where growth rate is insensitive to variations in temperature and flow.

the lower two profiles could easily be due to measurement error. Thus, to obtain uniformly doped layers it is clearly desirable to grow under conditions where the growth rate, and thus the transfer ratio, is insensitive to small variations of the growth parameters.

C. M. Wolfe
G. E. Stillman
W. T. Lindley

D. INFRARED TRANSMISSION, MAGNETIC BIREFRINGENCE, AND FARADAY ROTATION IN EuO

Infrared transmission, magnetic birefringence, and Faraday rotation have been measured in single crystals of EuO as a function of temperature and magnetic field in the wavelength region between 1.5 and 20 μ. The most transparent samples have an absorption coefficient at 20°K less than 0.5 cm^{-1} in the range between 2.5 and 9 μ, and less than 1.0 cm^{-1} at 10.6 μ. At 20°K and 9 kG, the Faraday rotation varies from 660 deg/cm at 10.6 μ, to 3×10^4 deg/cm at 2.5 μ, and over 10^5 deg/cm at 1.5 μ.

Section I

The europium chalcogenides EuO, EuS, and EuSe are semiconductors, ferromagnetie at low temperatures and are relatively transparent in certain wavelength regions. EuO becomes ferromagnetic below 77 °K with a saturation moment of close to 7 μ_B (Ref. 8), and has an energy gap[9,10] of 0.95 eV at 20 °K. There are very large magneto-optieal effects in these materials,[11-16] which have been studied rather extensivcly in the wavelength rangc below 1.2 μ corresponding to photon energies in the vicinity of and greater than the optical energy gap. Magnetie linear birefringenee and Faraday rotation have becn observed[12] in EuSe at liquid hclium temperature in the range between 0.75 and 0.80 μ, where a rotation of between 1.0×10^5 and 1.4×10^5 deg/cm was measured in a magnetic field of 20 kG. This corresponds to a specific rotation per unit attenuation of between 360 and 390 deg/dB. The magnetic dichroism of EuSe has been measured[13] at 4.2 °K in magnetic fields up to 20 kG between 0.68 and 0.80 μ, and rather large effects were observed due to the magnctic splitting of the band edge. Recently, Faraday rotation in EuO films has been measurcd[16] in the wavelength range between 0.4 and 1.2 μ in magnetic fields up to 20.8 kG and over the temperature range between 5° and 75 °K. At 5 °K, a rotation of 4.9×10^5 deg/cm at 0.66 μ was observed which corresponds to a specific rotation per unit attenuation of about 1 deg/dB. Here we report measurements of infrared transmission and magneto-optical effeets in EuO in the wavelength range between 1.5 and 20 μ. To our knowledge, this is the first report of either transmission or magneto-optical measurements in any europium ehalcogenide beyond 1.2 μ.

The samples used in these measurements were cleaved from single crystals of EuO grown in a welded tungsten crucible from starting material consisting of Eu metal and Eu_2O_3 with a large metal excess. Thc erueible was heated to 2185 °C and cooled slowly with an initial rate of approximately 3.3 °C per hour. The resulting crystal was mostly single, and samples up to several millimeters on a side could be cleaved from single-crystal sections. The eleaved samples were lapped to the appropriate thickness and polished using diamond paste. In the lapping and polishing steps, the samples were at all times immersed in methanol to prevent oxidation of the surface. This occurs very readily upon exposure to air or water vapor, and results in a pitted surfaee and a deterioration of the optical properties.

The infrared transmission, magnetic birefringence, and Faraday rotation of the EuO single erystals, in the wavelength range between 1.5 and 20 μ, have been studied as a function of temperature between 5° and 200 °K and in magnetic fields up to 9 kG. At 20 °K and 9 kG, the magnetic linear birefringence increases from a roughly constant value of $n_\perp - n_{||} = 1.07 \times 10^{-2}$ for wavelengths beyond 7 μ, to greater than 3.3×10^{-2} at 1.5 μ. The sign of the birefringence was determined by direetly observing the shift in the interferenee fringes in thin samples for E || H and E ⊥ H. Although the magneto-optical effects are strongest below the Curie point, measurable effeets persist at least up to 150 °K. The temperature and magnetic field dependences of the magnetie linear birefringenee and Faraday rotation will be presented in more detail in a forthcoming publication.

Figure 1-5 shows the transmission spectrum of an EuO sample 1.66 mm thick at 20 °K in a magnetic field of 9 kG. The field was applied in order to eliminate the effeets of domain scattering[17] which considerably reduce the transmission, especially at shorter wavelengths. We have plotted percent transmission instead of absorption coefficient since the reflection losses have so far varied too greatly from sample to sample, with nominally the same surfaee preparation, to

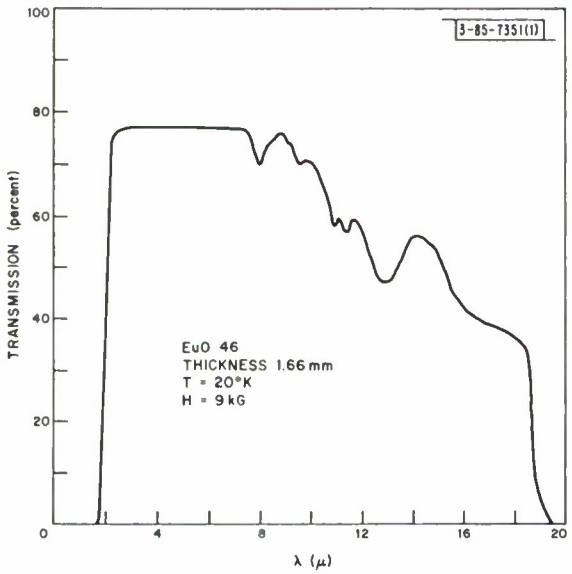

Fig. I-5. Infrared transmission of EuO.

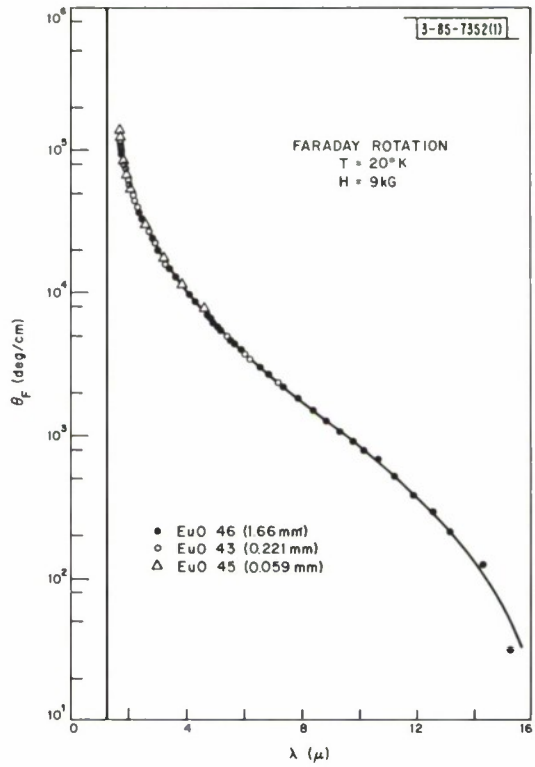

Fig. I-6. Infrared Faraday rotation of EuO.

yield reliable absorption coefficient data. The transmission between 3 and 7 μ is probably totally reflection limited. If this is true and the measured transmission of 77 percent represents the reflection limit, we obtain an absorption coefficient at 10.6 μ of 0.85 cm^{-1}. The structure at the longer wavelengths may be due to lattice absorption, crystalline imperfections or even surface treatment, and is under investigation. The short wavelength absorption edge occurs due to the onset of electronic transitions across the energy gap as discussed above.

Figure I-6 shows the Faraday rotation vs wavelength between 1.5 and 16 μ. The points represent a composite of data taken on three samples of different thickness. The data at long wavelength were taken on the sample of Fig. I-5. Due to the low applied field of 9 kG, the sample magnetization was not saturated and thus each sample experienced a different demagnetizing field, depending on its shape. Consequently, the measurements made on the thinner samples at the shorter wavelengths were scaled such that their long wavelength measurements agreed with those made on the thicker sample which had a cross section of 6.1 by 2.6 mm. Faraday rotation increases very rapidly at short wavelengths, reaching values in excess of 10^5 deg/cm in the vicinity of the band gap at 1.3 μ which is indicated by the vertical line. The maximum specific rotation per unit attenuation occurs at about 2.5 μ and is in excess of 1.4×10^4 deg/dB. The rotation of 660 deg/cm observed at 10.6 μ corresponds to a specific rotation per unit attenuation in excess of 150 deg/dB at this wavelength. The sign of the rotation is positive according to the convention outlined by Dillon.[18]

It is interesting to compare these results with those obtained both on EuO at shorter wavelengths noted above and on other materials in the infrared. Dillon has surveyed the work done up

to the fall of 1967 at wavelengths shorter than 2.5 μ. Notable are the results on EuSe mentioned above and on YIG, both of which have large values of specific rotation per unit attenuation. At 300°K, YIG has a specific rotation per unit attenuation of 800 deg/dB at 1.2 μ, and at least 325 deg/dB at 2.5 μ (Ref. 19). However, YIG absorbs rather strongly at wavelengths beyond 5 μ, and at 10.6 μ the absorption coefficient is about 115 cm^{-1} (Ref. 20). Consequently, the specific rotation per unit attenuation of YIG at this wavelength is less than $\frac{1}{4}$ deg/dB. To our knowledge, the only other magnetic material which has a measured Faraday rotation in the long wavelength infrared region is $CdCr_2Se_4$. Bongers and Zanmarchi[21] have measured the absorption coefficient and Faraday rotation of this material at 82°K and 15 kG between 1.17 and 18 μ. The Faraday rotation rises to over 9×10^3 deg/cm at the short wavelength end, and is 1.7×10^3 and -1.0×10^2 deg/cm at 2.5 and 10.6 μ, respectively. From their absorption measurements, this corresponds to 19.6 and −1.77 deg/dB at these two wavelengths, respectively. Recall that the corresponding values for EuO at 20°K are 3×10^4 and 660 deg/cm and 1.4×10^4 and 150 deg/dB.

We have emphasized above the magnitude of the Faraday rotation and of the specific rotation per unit attenuation. These figures are quite large in EuO in the range between 2.5 and 10.6 μ, indicating that this material may be quite useful for making infrared circulators and isolators in this wavelength region. In addition to the practical aspects, measurements of the magneto-optical properties of EuO in the infrared should shed some light on the conductivity processes in doped EuO and on the band structure and electronic properties of the europium chalcogenides.

J. O. Dimmock
C. E. Hurwitz
T. B. Reed

REFERENCES

1. Solid State Research Report, Lincoln Laboratory, M.I.T. (1968:3), p. 1.
2. J.R. Knight, D. Effer, and P.R. Evans, Solid State Electron. 8, 178 (1965).
3. C.M. Wolfe, A.G. Foyt, and W.T. Lindley, Electrochem. Technol. 6, 208 (1968), DDC 673592.
4. R.N. Hall, J. Phys. Chem. 57, 836 (1953).
5. M.D. Banus and H.C. Gatos, J. Electrochem. Soc. 109, 829 (1962).
6. F.V. Williams, J. Electrochem. Soc. 111, 886 (1964).
7. H. Brooks, Advan. Electron. and Electron Phys. 7, 158 (1955).
8. B.T. Matthias, R.M. Bozorth, and J.H. Van Vleck, Phys. Rev. Letters 7, 160 (1961).
9. G. Busch, P. Junod, and P. Wachter, Phys. Letters 12, 11 (1964).
10. G. Busch and P. Wachter, Phys. Kondens. Mat. 5, 232 (1966).
11. J.C. Suits and B.E. Argyle, J. Appl. Phys. 36, 1251 (1965).
12. _____, Phys. Rev. Letters 14, 687 (1965).
13. B.E. Argyle, J.C. Suits, and M.J. Freiser, Phys. Rev. Letters 15, 822 (1965).
14. J.H. Greiner and G.J. Fan, Appl. Phys. Letters 9, 27 (1966).
15. S. Methfessel, M.J. Freiser, G.D. Pettit, and J.C. Suits, J. Appl. Phys. 38, 1500 (1967).
16. K.Y. Ahn and J.C. Suits, IEEE Trans. Magnetics MAG-3, 453 (1967).
17. J.C. Suits, J. Appl. Phys. 38, 1498 (1967).
18. J.F. Dillon, Jr., J. Appl. Phys. 39, 922 (1968).
19. R.C. LeCraw, D.L. Wood, J.F. Dillon, Jr., and J.P. Remeika, Appl. Phys. Letters 7, 27 (1965).
20. D.L. Wood and J.P. Remeika, J. Appl. Phys. 38, 1038 (1967).
21. P.F. Bongers and G. Zanmarchi, Solid State Commun. 6, 291 (1968).

II. OPTICAL TECHNIQUES AND DEVICES

A. INFRARED DETECTOR AND CIRCUIT FREQUENCY RESPONSE MEASUREMENTS

We have made direct measurements of the frequency response from 10 to 1000 MHz of two Ge:Cu photoconductors and their associated circuitry using a heterodyne procedure employing a stable, single-frequency CO_2 laser and a current-tunable $Pb_{0.88}Sn_{0.12}Te$ diode laser.[1] Both lasers emit radiation of wavelength near 10.6 μ. The photoconductors, cooled to liquid helium temperature, have carrier lifetimes near 2×10^{-10} sec to give a cutoff frequency of approximately 1200 MHz. Each detector was shunted by a 50-ohm metal film load resistor inside the dewar with the signal coupled by a miniature stainless-steel coaxial 50-ohm line to an electrical feedthrough at the dewar wall. A standard bias "tee," isolating the detector bias supply from the high-frequency signal, was connected to the coaxial line outside the dewar and coupled the signal to a low-noise amplifier driving a wide-band spectrum analyzer. During these experiments, two low-noise amplifiers were used to cover the frequency range: one having a bandpass of 10 to 400 MHz, the other from 400 to 1000 MHz.

The diode laser emission remained essentially constant during the current-tuning over the 1000-MHz beat frequency range required for these measurements, as confirmed by identical frequency response curves generated whether the diode laser frequency was above or below the CO_2 laser frequency. However, the combination of the bias "tee" and amplifier produced up to 3-dB variation in the electrical flatness with frequency, and, although the detector response followed these variations to a large extent, no quantitative conclusions should be drawn until the high-frequency characteristics of the bias "tee" have been improved. In this work, a constant level of CO_2 laser illumination has been used; future experiments will study the effects of different power levels, as well as of different applied electric fields on the detector.

E. D. Hinkley
H. A. Bostick

B. SHORT-TERM STABILITY MEASUREMENTS OF 100-WATT CO_2 MASTER OSCILLATOR POWER AMPLIFIER (MOPA) SYSTEM

The individual characteristics of the 9-meter CO_2 amplifier and the single-frequency stable oscillator have been described previously.[2,3] Here, we shall discuss some preliminary short-term stability measurements of the MOPA combination at the Lexington Field Station.

In these measurements, first the output of the master oscillator was heterodyned with another stable single-frequency reference laser and the beat-frequency spectrum was observed with the amplifier on and off. Since there was no change in the appearance of the beat frequency spectra under these conditions, feedback apparently did not cause any instability under CW operation of the amplifier. Figure II-1 shows a typical spectrum analyzer display of the beat frequency between the master and reference oscillators with the amplifier in operation.

The reference laser output was heterodyned with the amplifier output in the next set of measurements. The beat frequency spectra were observed with both sealed-off and flowing-gas operation of the amplifier. These measurements showed no significant deterioration of the beat

-SS-7368

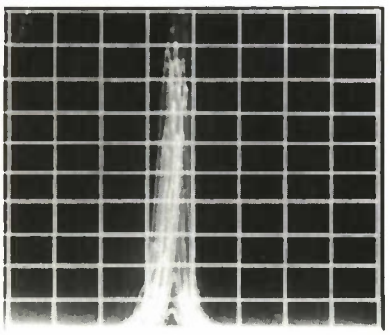

Fig. II-1. Spectrum analyzer display of beat frequency af reference laser and master oscillator with amplifier in operatian:

Film exposure time	1 sec
Horizontal scale	10 kHz/cm
Vertical scale	Linear
Scanning rate	60/sec

-SS-7369

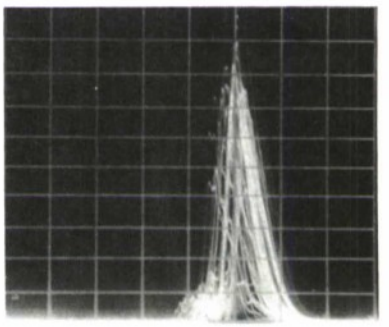

Fig. II-2. Spectrum analyzer display of beat frequency of reference laser and output of amplifier in sealed-off operatian:

Film expasure time	1 sec
Horizontal scale	5. 5 kHz/cm
Vertical scale	Linear
Scanning rate	60/sec

-SS-7370

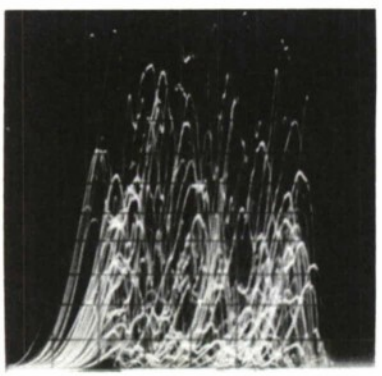

Fig. II-3. Spectrum analyzer display af beat frequency of reference laser and output of amplifier in flowing-gas operation:

Film exposure time	1 sec
Horizontal scale	10 kHz/cm
Vertical scale	Linear
Scanning rate	60/sec

frequency spectrum in sealed-off operation. However, with flowing-gas operation of the amplifier, the envelope of the beat frequency spectrum broadened by about an order of magnitude from 5 to 50 kHz for 1-sec observation time. Figures II-2 and II-3 show the spectrum analyzer displays of the beat frequency with sealed-off and flowing-gas operation of the amplifier, respectively. The output power of the amplifier was about 70 W both in sealed-off and flowing-gas operation. The amplifier output dropped to zero with the input oscillator off, indicating the absence of spurious self-oscillation.

The broadening of the output spectrum shown by Fig. II-3 could be caused by index variation of the flowing gas and acoustic modulation due to vibrations of the vacuum pumps. It should be noted that no real effort was made toward acoustic and vibrational isolation of the MOPA system, since more detailed stability experiments are planned after installation at the permanent site.

R. J. Carbone
C. Freed

C. STABLE LASER OSCILLATOR: DESIGN AND TESTING

Several units of the redesigned version of the stable laser oscillator have been assembled and tested. The preliminary stability measurements of these units have indicated that the expected improvements in short-term stability will be achieved in addition to the significantly improved ease of assembly, operation, and reduced cost of the new units.

C. Freed

D. GAIN SATURATION AND DIFFUSION IN CO_2 LASERS

Experiments have been carried out to determine the effects of molecular diffusion on the saturation parameter of the CO_2 laser. The detailed analysis and description of this work has been submitted[4] to the Department of Electrical Engineering in partial fulfillment of the requirements for the degree of Master of Science. The abstract of an abbreviated version of this work which has been submitted for publication follows:

> "The effect of rotational-vibrational relaxation and molecular diffusion on the saturation parameter of the CO_2 laser is investigated experimentally.
>
> "A summary is presented of how the theory of two-level systems can be extended to a multilevel laser system like CO_2. The rate of relaxation of the upper levels, using published experimental results, is such as to suggest that diffusion effects may play an important role in laser beams with radii of less than a few millimeters.
>
> "For experimental verification of the diffusion hypothesis, the gain of a sealed CO_2 amplifier is measured as a function of input power for four different beam radii. The equivalent saturation parameter derived from these measurements decreases monotonically from 97 w/cm^2 to 25 w/cm^2 as the average input beam radius increases from 0.9 mm to 2.5 mm in the 9 mm radius discharge tube of the amplifier."

C. P. Christensen, Jr.†
C. Freed
H. A. Haus†

† Department of Electrical Engineering, Massachusetts Institute of Technology.

E. ABSORPTION OF CO_2 LASER RADIATION BY H_2O VAPOR

The transmission of the atmosphere for the P(18) and P(22) lines of a CO_2 laser has been measured over a 1.3-km path for partial pressures of H_2O vapor ranging from 10 to 25 mb. Although the detailed analysis of the data is not complete, sample calculations indicate that the absorption coefficient for 10.57- and 10.61-μ radiation in a 300°K atmosphere is about 1.8×10^{-7} cm^{-1} mb^{-1}. This corresponds to a mass absorption coefficient of 0.24 $cm^2 g^{-1}$, or to a loss factor of 0.08 dB km^{-1} mb^{-1}. From measurements of atmospheric absorption of solar radiation, it had been estimated by Long[5] that the mass absorption coefficient is 0.15 $cm^2 g^{-1}$. No difference was observed between the absorptions for the two wavelengths. There was surprisingly little correlation between visibility and the infrared transmission for visibilities of 2 to 20 miles.

T. J. Gilmartin

F. OPTICAL HETERODYNE DETECTION

It has been asserted that the effective antenna aperture of an optical heterodyne detector is independent of detector position in the combined signal-local oscillator beam.[6] While this is a good approximation in most experimental situations, it is not correct when the detector is displaced a distance large compared with c/ν_d, where ν_d is the frequency difference between signal and local oscillator. An integral expression has been derived for the effective quantum efficiency η_{eff} in terms of the two field distributions over angle, and explicit expressions have been derived for several special cases. In particular, the depth of the region of large efficiency near the focus of a lens imaging coaxial signal and local oscillator plane waves was found to be approximately

$$z_o = 16 f^{*2} \lambda_d$$

where f^* is the f-number of the lens (= focal length/diameter), and

$$\frac{1}{\lambda_d} = \left| \frac{1}{\lambda_s} - \frac{1}{\lambda_o} \right|$$

is the difference in wave number between signal and local oscillator.

A. H. M. Ross

G. A MEASUREMENT OF PHASE FLUCTUATIONS IN ATMOSPHERIC PROPAGATION

When a small-aperture telescope views a distant object, wavefront distortions which are introduced by atmospheric inhomogeneities cause the image to wander in the focal plane of the telescope. The displacement of this image from the optical axis can be measured directly when the object is being tracked and the optical axis is fixed with respect to the object. When two small apertures have a common focus and the image from each is characterized by an rms displacement δ, then the rms displacement that will be measured when both apertures are open will be $\sqrt{2}\delta$ when the wavefront distortions at the two apertures are uncorrelated, and 2δ when they are completely correlated. By placing two small movable apertures in front of a large-aperture tracking telescope, the correlation function for the phase fluctuations can be measured. Furthermore, the amount of phase modulation over the wavefront can be determined:

$$\Delta\varphi \sim \frac{2\pi \ell_c}{\lambda} \frac{\delta}{f}$$

where $\Delta\varphi$ is the phase fluctuation, ℓ_c is the measured correlation length, f is the telescope focal length, and λ is the wavelength.

Preliminary measurements in the 8- to 12-μ region have been made using the infrared tracking system. The effect is observable, but not dramatic; that is, less than 10-percent difference in rms tracking error was observed when two 1-inch apertures were placed 1 inch and then 20 inches apart while viewing an infrared source at a distance of 3 miles. More measurements are planned with slightly larger apertures arranged in a geometry which will allow separate measurement of the correlation of the azimuth and elevation components of the image displacement vector.

T. J. Gilmartin
P. R. Longaker

REFERENCES

1. Solid State Research Report, Lincoln Laboratory, M.I.T. (1968:3), p. 19.
2. Ibid., p. 17.
3. C. Freed, IEEE J. Quant. Electron. QE-4, 404 (1968).
4. C.P. Christensen, Jr., Thesis, Department of Electrical Engineering, M.I.T. (September 1968).
5. R. Long, Summary of Some Aspects of Atmospheric Propagation, Third DOD Conference on Laser Technology, compiled by: The ElectroScience Laboratory, Ohio State University, Columbus, Ohio (April 1967).
6. A.E. Siegman, Appl. Opt. 5, 1588 (1966).

III. MATERIALS RESEARCH

A. PROPOSED SCALE FOR OXYGEN AFFINITY OF METALS

In dealing with the reactions of metals and their oxides, it would be useful to have a numerical scale which characterizes oxygen affinity in the way that the electronegativity scale and the pH scale characterize electron affinity and hydrogen ion affinity, respectively. We have constructed such an oxygen affinity scale, as given in Table III-1, by arranging the metals (plus hydrogen and carbon) in increasing order of their "pO" values, where pO is defined as the negative common logarithm of the oxygen pressure (in atmospheres) which is in equilibrium with metal and its lowest oxide at 1000°K. These values were calculated from the data contained in Ref. 1.

Although the correlation between oxygen affinity and pO is not perfect, in general oxygen affinity increases with increasing pO, since for most metals pO is directly proportional to the free energy of the following reaction at 1000°K:

$$\frac{2}{n} M + O_2 \rightarrow \frac{2}{n} MO_n \quad . \tag{III-1}$$

The free energy of this reaction is given by $\Delta G = -RT \ln p_{O_2} = 1000(2.303R)pO$, provided that oxygen is the only volatile species. This is the case at 1000°K with a few exceptions, as noted in Table III-1. If the metal and its oxide are both gaseous, $\Delta G = 1000(2.303R)pO(p_{MO_n}/p_M)^{2/n}$. If oxygen is the only volatile species in Reaction (1),

$$-\log p_{O_2}(T) = \frac{\Delta G}{2.303RT} = \frac{1}{2.303R}\left(\frac{\Delta H}{T} - \Delta S\right) \quad . \tag{III-2}$$

For most of the metals in Table III-1, $\Delta S = 45 \pm 10$ e.u. For $\Delta S = 45$ e.u., the variation of $-\log p_{O_2}(T)$ with reciprocal absolute temperature is shown in Fig. III-1 for various values of pO ($\equiv -\log p_{O_2}$ at $10^3/T = 1$). It is seen that the rank order of $-\log p_{O_2}$ values at any temperature is the same as the rank order of pO values. Furthermore, since the temperature dependence of $-\log p_{O_2}$ does not depend strongly on ΔS, for most of the metals in Table III-1 the order of increasing oxygen affinity at any temperature is nearly the same as the order of increasing pO.

For a metal whose value of ΔS in Reaction (1) differs from 45 e.u., the values of $-\log p_{O_2}(T)$ may be found by drawing a straight line between the point at $10^3/T = 1$ corresponding to pO for the metal, and the point on the ordinate corresponding to the appropriate value of ΔS. However, this procedure is valid only if the temperature range covered does not include the boiling point of either the metal or its oxide.

The main application of the pO scale of Table III-1 is to predict the course of oxidation-reduction reactions. Since a metal will reduce the oxides of metals whose pO values are sufficiently smaller than its own, the metals used commercially for reduction processes are those with high pO values (e.g., Ca, Mg, and Al). The pO scale can also be used to predict which reactions will not proceed. This information is necessary in selecting compatible materials for use as crucibles at high temperatures. Metal crucibles are used to contain molten oxides, which would tend to dissolve oxide crucibles. In order to avoid reaction, it is necessary to select a

TABLE III-1
OXYGEN AFFINITY OF METALS

Oxide	pO†	−ΔS (e.u.)	Oxide	pO†	−ΔS (e.u.)
Hg_2O‡	−6.5	94	WO_2	21.2	38
Au_2O_3	−5.5	25	K_2O	23.2	66
Ag_2O_3	−3.3	30	In_2O_3	24.1	50
PtO	−1.3	42	ZnO	25.8	47
PdO	−1.1	48	Ga_2O_3	26.2	51
IrO_2	0.9	40	No_2O	28.9	68
RuO_2§	2.8	14	P_2O_3	29.7	36
Rh_2O	4.2	22	Cr_2O_3	30.1	41
O_sO_4§	5.0	17	MnO	32.6	35
TeO_2	7.2	42	Ta_2O_5	33.2	42
Tl_2O§	8.1	8	NbO	33.7	36
Cu_2O	9.6	33	VO	34.5	40
BiO	11.4	55	B_2O_3	35.4	33
PbO	12.7	46	SiO_2	36.3	43
TcO_2	13.6	42	TiO	44.2	44
ReO_2	13.6	39	RaO	46.3	48
As_2O_3¶	14.9	25	Al_2O_3	47.2	51
Sb_2O_3	15.3	40	ZrO_2	47.2	41
Cs_2O‡	15.3	72	HfO_2	48.1	45
CaO	16.2	42	Li_2O	48.5	70
NiO	16.2	42	BaO	48.6	42
CdO	16.6	50	Sc_2O_3	50.3	51
GeO_2	18.4	45	SrO	51.2	44
Rb_2O¶	19.0	126	BeO	52.0	47
SnO_2	19.7	50	MgO	52.0	55
H_2O¶	20.1	26	Y_2O_3	52.0	44
(Range)	(16-24)	–	$(RE)_2O_3$	53.3	43
MoO_2	20.1	38	ThO	55.5	43
FeO	20.6	32	CoO	55.5	50
Co§	21.0	−41	Ac_2O_3	56.4	38

† $pO = -\log p_{O_2}$ for oxygen in equilibrium
‡ Metal gaseous
§ Oxide gaseous
¶ Metal and oxide gaseous

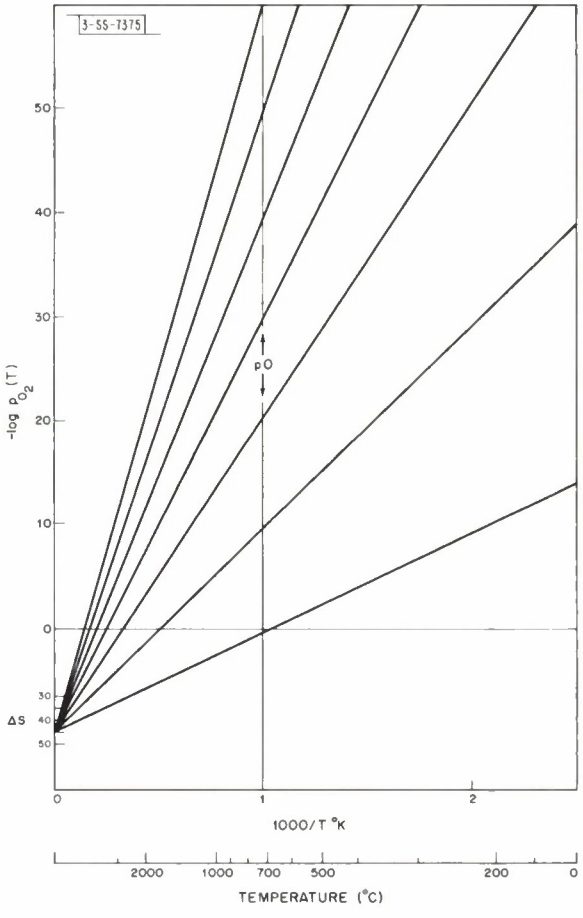

Fig. III-1. Variatian af (–lag p_{O_2}) with recipracal absalute temperature, where p_{O_2} is partial pressure af O_2 (in atmaspheres) in equilibrium with a metal and its lawest axide. Far lines shawn, $\Delta S = 45$ e.u. far reactian $2/nM + O_2 \rightarrow 2/nMO_n$.

metal whose pO is lower than that of the oxide. Platinum is widely used because of its low pO, but it suffers from a relatively low melting point and high cost. Recently, iridium has found considerable use at the higher temperatures required for growth of such oxides as sapphire, ruby, and yttrium aluminum garnet. However, it must have a moderate amount of protection from the atmospherc because it has a volatile oxide. We have used both open and sealed tungsten and molybdenum crucibles to contain molten Al_2O_3 and EuO. Although tantalum is commonly used to contain rare-earth oxides because it is very malleable and easily fabricated, it is the most reactive of these crucible materials. Recently, rhenium has become easily available, and its low pO suggests that it should be a good crucible material.

Oxide crucibles are used to contain molten metals, which would tend to alloy with other metals. The usual choices are SiO_2, Al_2O_3, ZrO_2, BeO, MgO, ThO, and CaO. It can be seen from Table III-1 that these oxides are among the most stable.

T. B. Reed

B. LIQUIDUS SURFACE IN Zn-Cd-Te SYSTEM

In recent experiments, we have grown $Zn_xCd_{1-x}Te$ alloy crystals from stoichiometric melts by thc Bridgman method or from Te solutions by the temperature gradient solution zoning technique developed for ZnTe (Ref. 2). Good control of crystal composition and homogeneity requires

TABLE III-2
LIQUIDUS TEMPERATURES IN THE Zn-Cd-Te SYSTEM

Section	Composition			Supercooling (°C)	Temperature (°C)	Reproducibility (°C)
	Zn	Cd	Te			
CdTe-ZnTe	0.10	0.40	0.50	0	1121.6	±0.6
	0.175	0.325	0.50	0	1144.5	–
	0.20	0.30	0.50	2.4	1156.6	–
	0.30	0.20	0.50	0	1198.1	–
	0.40	0.10	0.50	0	1244.9	±0.2
ZnTe-Te	0.40	0	0.60	0	1164.7	±0.3
	0.30	0	0.70	0	1060.5	–
	0.20	0	0.80	0	967.7	±0.3
	0.10	0	0.90	0	869.5	–
Cut A: $(Zn_{0.80}Cd_{0.20})_{1-x}Te_x$	0.32	0.08	0.60	0	1124.8	±0.3
	0.24	0.06	0.70	0	1027.7	–
	0.16	0.04	0.80	0.5	927.4	–
Cut B: $(Zn_{0.50}Cd_{0.50})_{1-x}Te_x$	0.45	0.45	0.10	0	1043.5	±0.3
	0.35	0.35	0.30	0	1111.7	±0.1
	0.20	0.20	0.60	0	1052.5	±0.7
	0.15	0.15	0.70	0	959.2	±0.1
	0.10	0.10	0.80	0	870.5	–
	0.05	0.05	0.90	2.7	770.7	–
Cut C: $(Zn_{0.20}Cd_{0.80})_{1-x}Te_x$	0.18	0.72	0.10	0	969.8	±0.1
	0.14	0.56	0.30	0	1045.5	±0.7
	0.08	0.32	0.60	0	992.8	±0.8
	0.06	0.24	0.70	2.7	902.0	–
	0.04	0.16	0.80	0	819.4	–
CdTe-Te	0	0.50	0.50	0	1092.0	±0.2
	0	0.40	0.60	0	967.4	–
	0	0.30	0.70	0	879.2	–

a knowledge of solid-liquid phase equilibria in the Zn-Cd-Te ternary system more precise than is now available. To obtain this information, liquidus temperatures in the system have been determined by differential thermal analysis. Major efforts have been directed toward a precise determination of temperatures along the pseudo-binary CdTe-ZnTe liquidus line and over the Te-rich region of the ternary liquidus surface. Because of significant discrepancies in published data,[3-5] the Te-rich halves of the Cd-Te and Zn-Te liquidus curves have been redetermined. Finally, the Te-deficient side of the ternary surface has been surveyed to obtain an overall representation of the ternary phase diagram.

In the differential thermal analysis (DTA) experiments, particular care was taken to approximate equilibrium conditions at the onset of freezing. This was achieved by cooling melts of only slightly superheated high-purity materials at sufficiently low rates to avoid appreciable supercooling. Table III-2 lists the liquidus temperatures obtained for the pseudo-binary CdTe-ZnTe system, the Te-rich side of the Cd-Te and Zn-Te binary systems, and cuts A, B, and C of the ternary system corresponding to Cd/Zn ratios of 0.25, 1.00, and 4.00, respectively. When repeated runs were made without supercooling, the reproducibility of the liquidus temperatures was usually well within ±1 °C, as listed in Table III-2.

Both CdTe and ZnTe solidify in the cubic zinc-blende structure, and they form a complete series of solid solutions. The pseudo-binary CdTe-ZnTe liquidus curve (Fig. III-2) is consistent with complete solid solubility. The sublinear variation in temperature along the liquidus, however, was unexpected and suggests a tendency toward segregation in the liquid. The relatively low liquidus temperatures also indicate the possibility of growing high Zn content alloy crystals from stoichiometric melts in quartz ampoules. Figure III-2 also shows liquidus lines for four other constant Te concentrations, each of which exhibits a similar sublinear increase in temperature from the Cd-Te to the Zn-Te system.

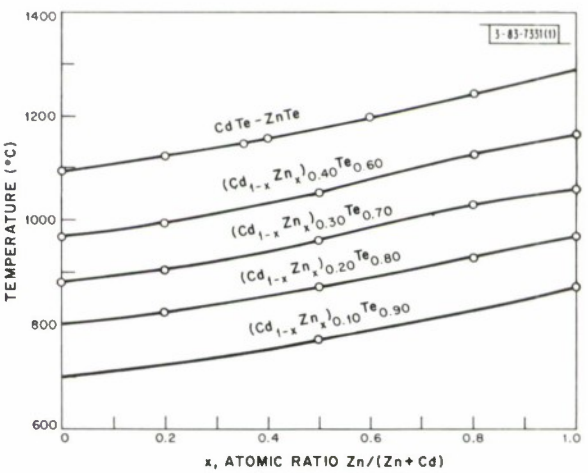

Fig. III-2. Liquidus curve for pseudo-binary CdTe-ZnTe system.

The liquidus curves on the Te-rich side of the Cd-Te and Zn-Te binary systems are presented in Fig. III-3. For both systems, the arrest temperatures previously determined by Kulwicki[3] are significantly higher than the present results, probably because his arrests were determined on heating curves. For nonstoichiometric compositions, this method is less sensitive than the cooling technique and can yield values which are too high. On the other hand, the data of Carides and Fischer[4] are significantly lower due to their use of high cooling rates. Best agreement is observed with the data of Lorenz[5] for the Cd-Te system and of Strauss[6] for the Zn-Te system. Both of these investigators used slow cooling techniques and minimized supercooling.

Each of the five liquidus curves on the Te-rich side of the ternary system (Fig. III-4), for cuts A, B, and C and for the binary systems Cd-Te and Zn-Te, exhibits an inflection point,

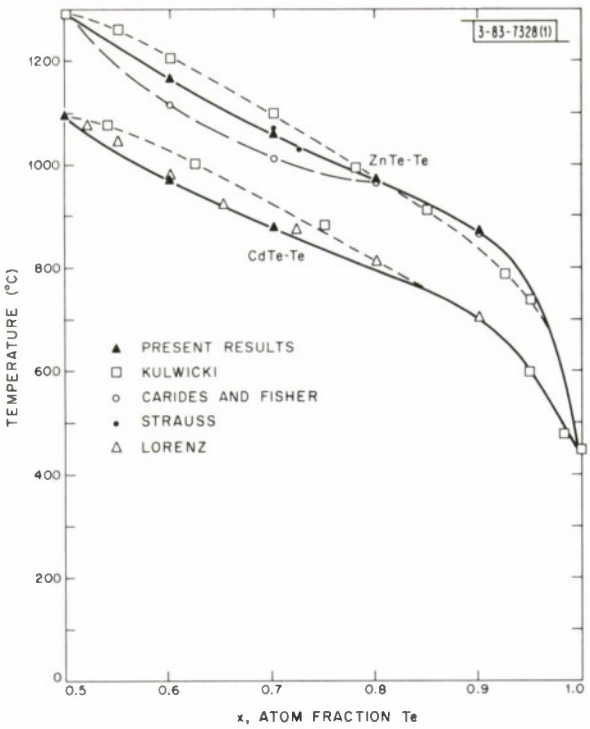

Fig. III-3. Liquidus curves for ZnTe-Te and CdTe-Te systems.

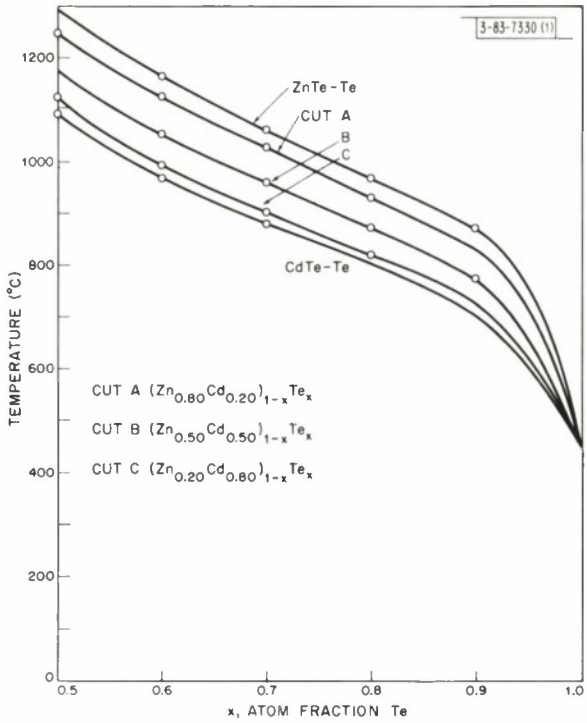

Fig. III-4. Liquidus curves for Te-rich compositions in Zn-Cd-Te system.

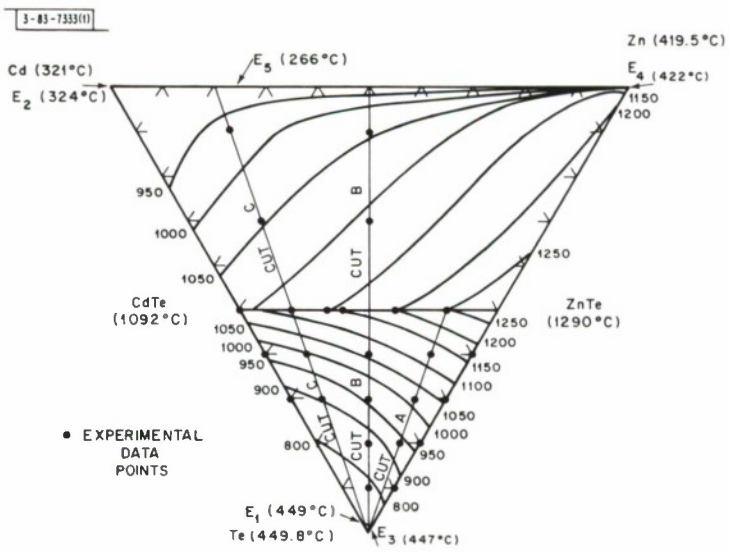

Fig. III-5. Liquidus isotherms for Zn-Cd-Te system.

indicating a tendency toward formation of two liquid phases. This tendency is even more evident in the Cd-Se (Ref. 7) and Hg-Se (Ref. 8) systems which actually show monotectic transformations on the Se-rich side of the phase diagrams.

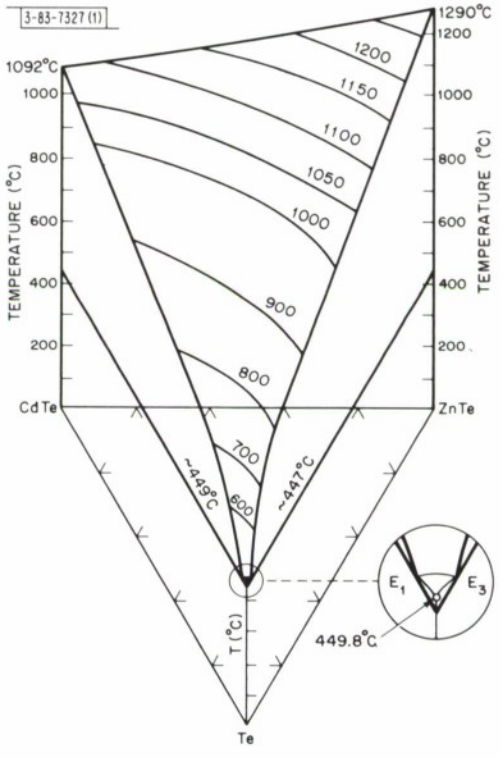

Fig. III-6. Isometric spatial representation of Te-rich region of Zn-Cd-Te phase diagram.

Isothermal liquidus points in the ternary system have been obtained by interpolation along cuts A, B, and C (Fig. III-4) and the three limiting liquidus lines (Figs. III-2 and III-3). The resulting isotherms are presented in the ternary phase diagram (Fig. III-5) and in the isometric spatial representation of the Te-rich region (Fig. III-6). The isotherms are characterized by peaks along the pseudo-binary CdTe-ZnTe line. This indicates significant association in the liquid between II and VI atoms, and corresponds to the sharp rise in temperature near stoichiometric composition that is observed in most II-VI binary phase diagrams. The binary eutectic temperatures in the Cd-Te and Zn-Te binary systems[2] have also been indicated on the ternary phase diagram. These eutectics are almost completely degenerate; consequently, the ternary eutectic and the four boundary lines are also expected to be degenerate.

J. M. Steininger
D. Apelian
R. E. England

C. DIFFERENTIAL THERMAL ANALYSIS (DTA) AT LOW TEMPERATURES

A large number of electronic materials undergo structural or magnetic transition at low temperatures. Specific heat measurements have frequently been used to detect such transitions. Conventional adiabatic techniques[9] are, however, laborious. Continuous-heating calorimetry[10] also requires adiabatic conditions, which are difficult to achieve and maintain. X-ray diffraction experiments are even more time consuming, requiring point-by-point measurements, and cannot detect purely magnetic transitions.

DTA[11] is widely used to detect phase transitions above room temperature, but is rarely used below room temperature. It does not yield quantitative specific heat values, but in many cases only the general shape of the specific heat curve is required. The difficulties associated with using DTA at low temperatures are: (1) The lattice specific heat of most materials changes rapidly with temperature so that a reference material of similar specific heat to that of the specimen is not available; (2) the thermal conductance within a powder sample and between the sample and thermocouple is poor; (3) the transitions of interest are usually second order and the specific heat changes are small; and (4) transformation kinetics are frequently slow.

We have developed a system which overcomes these difficulties sufficiently to permit use of DTA to detect low-temperature transitions. The experimental arrangement is shown in Fig. III-7. The specimen is a pellet consisting of approximately 1 gm of powder pressed around a 5-mil copper-constantan thermocouple. This pellet is separated from a massive copper block by a thick fused quartz sleeve so that the thermal conductance of the sleeve K_R is much less than that of the specimen K_s. A second thermocouple senses the temperature of the block, which serves as the reference. The specimen thermocouple is coiled inside the quartz sleeve to avoid thermal shorting of the specimen and block. Both thermocouples are thermally anchored to the outside of the block.

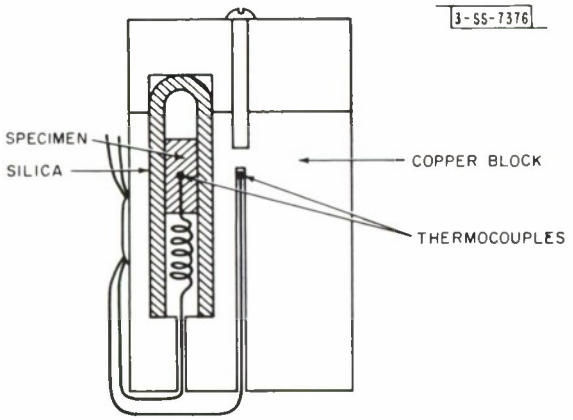

Fig. III-7. Sample holder for DTA measurements at low temperatures.

The block is heated or cooled at a constant rate of 0.2° to 0.5°K/min in a controlled temperature dewar using helium as an exchange gas. The specimen can be swept through the temperature range 15° to 400°K in this way. Typically, the temperature difference ΔT between the specimen and block is 0.1° to 0.5°K. This temperature difference is amplified and recorded as a function of T on an x-y recorder. Under these conditions, $C_{ps} = K_R \Delta T/S$, where C_{ps} is the heat capacity of the specimen, and S is the rate of change of specimen temperature, approximately equal to that of the block. Magnetic fields may be applied by a conventional electromagnet.

Figure III-8 shows a DTA curve obtained for CoS_2 in the vicinity of the Curie temperature (124°K). A typical λ-type anomaly is observed. For magnetic transitions, an external magnetic field can modify the shape of the curve, making it possible to distinguish these from structural transitions. Figure III-9 shows the result for $Sn_{0.8}Ge_{0.2}Te$, which undergoes a small rhombohedral distortion from cubic symmetry. The transition temperature of 180°K obtained by DTA is in good agreement with that obtained from x-ray diffraction experiments.[12]

At temperatures of 40° to 50°K, DTA results with the present apparatus are unreliable, because thermal effects due to the desorption of exchange gas or residual gases are observed. Heating the block itself directly in a good vacuum should overcome this problem.

F. T. J. Smith

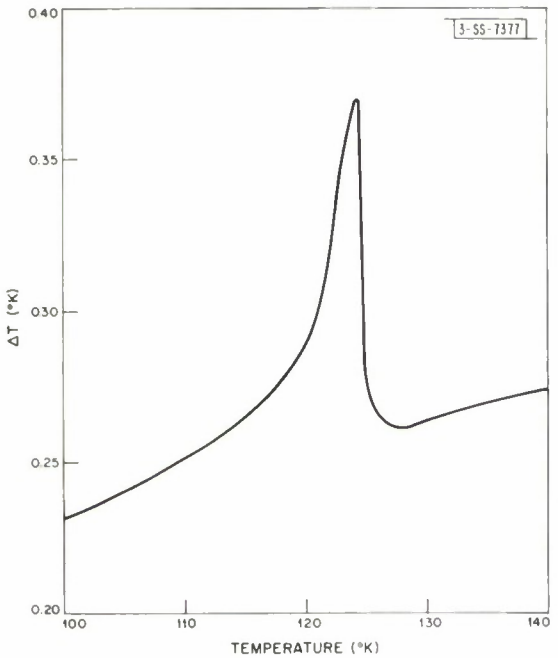

Fig. III-8. DTA curve for magnetic tronsition in CoS_2 (Curie temperoture of 124°K).

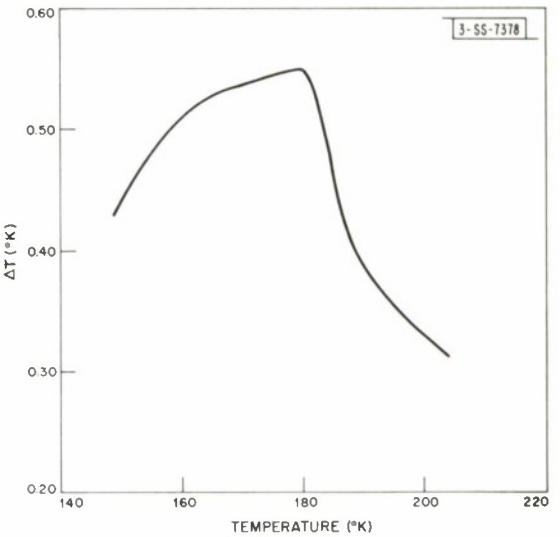

Fig. III-9. DTA curve for cubic-rhombohedrol tronsformotion in $Sn_{0.8}Ge_{0.2}Te$ at 180°K.

D. CRYSTAL GROWTH OF $Eu_{3-x}Gd_xFe_5O_{12}$ GARNETS

Single crystals of $Eu_{3-x}Gd_xFe_5O_{12}$ garnets up to 22 mm on a side have been grown from a $PbO-PbF_2-B_2O_3$ flux. The method used was essentially the same as Grodkiewicz, Dearborn, and Van Uitert[13] employed to grow $Y_3Fe_5O_{12}$ crystals, except that the Fe_2O_3 content of the melt was approximately doubled in order to prevent the formation of $EuFeO_3$ (Eu orthoferrite). The charge was heated to 1260°C in a platinum crucible under 1 atm of oxygen and then cooled at 1 deg/hr to 900°C, after which the flux was decanted.

Attempts have also been made to grow Eu garnet crystals out of molten Fe_2O_3 in order to reduce the foreign ion contamination generally resulting from use of the $PbO-PbF_2-B_2O_3$ flux. These experiments were performed under oxygen pressures of about 1500 psi in the high-pressure furnace that had been used to grow single crystals of ferrous-free $CoFe_2O_4$ (Ref. 14). These oxygen pressures did not prevent the decomposition of stoichiometric $Eu_3Fe_5O_{12}$ into $EuFeO_3$ and Fe_2O_3 at the temperature required for melting the charge. However, it was found that the garnet phase could be stabilized by using a large excess of Fe_2O_3, and that adding a small amount of $BaFe_{12}O_{19}$ lowered the melting temperature from slightly above 1600°C, to 1500° to 1575°C. When the melt was cooled at the rate of 2 deg/hr, very small crystals of Eu garnet (maximum dimension of 3 mm) were formed in a matrix of Fe_2O_3.

When a flux of pure $BaFe_{12}O_{19}$ (amounting to 30 percent by weight of the total charge) was employed, columnar garnet grains approximately 4 mm long were obtained. Since this attempt was unsuccessful, $BaFe_{12}O_{19}$ will be replaced by the lower melting $NaFeO_2$. We used this flux in growing $CoFe_2O_4$ crystals but abandoned it because traces of sodium (about 300 ppm) were detected in the crystals.

A. Ferretti
R. J. Arnott
E. J. Delaney

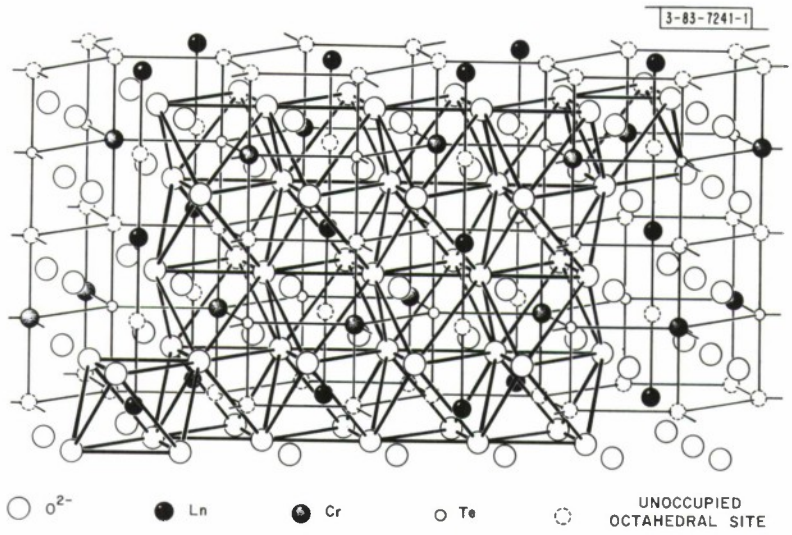

Fig. III-10. Crystal structure of $LnCrTeO_6$.

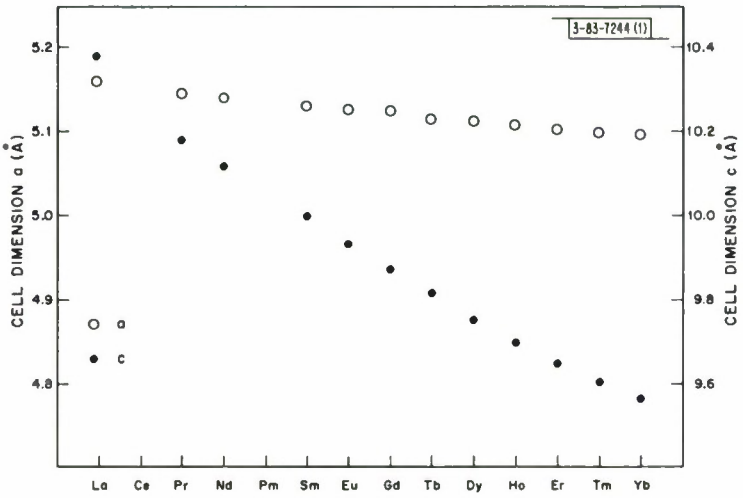

Fig. III-11. Cell dimensions a and c for $LnCrTeO_6$ compounds.

E. $LnCrTeO_6$ – A SERIES OF RARE-EARTH COMPOUNDS BASED ON THE $PbSb_2O_6$ STRUCTURE

The crystal structure of $PbSb_2O_6$ consists of a hexagonal close-packed oxygen array having alternate basal planes of octahedral interstices 2/3 filled by Sb^{5+} ions, and the interleaved planes of octahedral sites 1/3 filled with Pb^{2+} ions. The cations order within the planes, with the Sb^{5+} ions forming a simple hexagonal array with Pb^{2+} ions at the body center of each primitive Sb^{5+}-ion hexagon. In this arrangement, none of the cation-occupied oxygen octahedra share common faces. This $PbSb_2O_6$ structure is adopted by the antimonates $M^{II}Sb_2O_6$ (M^{II} = Ba, Sr, Ca, Hg, Cd, Pb) (Ref. 15) and the arsenates $M^{II}As_2O_6$ (M^{II} = Sr, Ca, Hg, Cd, Pb, Co, Ni) (Refs. 15 and 16). The properties of the Ni and Co arsenates stimulated interest in the structure and raised the question of whether further substitution of cations, especially magnetic cations, is possible. This study is concerned with the substitution of rare-earth cations Ln^{3+} for the Pb^{2+} of the $PbSb_2O_6$. Charge compensation then requires a simultaneous substitution of an M^{4+} ion for an Sb^{5+} ion, or an $M^{3+} + M^{6+}$ pair for two Sb^{5+} ions. The ions Sb^{5+} and Te^{6+} with noble gas configuration, and the ion Cr^{3+} are similar in showing a strong preference for regular octahedral coordination. Therefore, materials with the composition $Ln^{3+}Cr^{3+}Te^{6+}O_6$ were chosen for study.

Stoichiometric amounts of Ln_2O_3, Cr_2O_3, and TeO_2 were intimately mixed and fired for 2 hours at 1000°C. X-ray investigation of the resulting materials indicated that a new phase had been formed for Ln = La, Pr, Nd, Sm, Eu, Gd, Tb, Dy, Ho, Er, Tm, Yb, Y. The powder diagrams could be indexed essentially in analogy with $PbSb_2O_6$. However, there was an additional line which was weak for $LaCrTeO_6$ and which decreased in intensity for the heavier rare-earth compounds until it was barely perceptible for the Er, Tm, and Yb compounds. Since this line could not be related to an impurity, it seemed to be a superstructure line requiring an enlargement of the unit cell. Since simple ordering of Cr^{3+} and Te^{6+} ions within a basal plane would not enlarge the unit cell, a doubling of the c-axis was anticipated. This allowed indexing the additional line as 101, in agreement with the experimental data, and leads to a cation distribution with unlike near-neighbors within the Cr-Te layers and ordering between layers to form Cr^{3+}-Te^{6+}-Cr^{3+} columns along the c-axis (Fig. III-10). An intensity calculation for the ideal $LaCrTeO_6$ structure showed that the calculated intensity of the 101 superstructure line is much stronger than observed. This indicates that the layer sequence has some disorder.

The lattice constants were determined by the Straumanis technique. Figure III-11 shows their dependence on the rare-earth atom. The c-parameter depends much more strongly on the size of the rare-earth atom than does the a-parameter. This is consistent with the conclusion that in layer compounds of this type, the a-parameter is mainly determined by the complex-forming cations, whereas the c-parameter varies with the radius of the big, relatively ionic cation.

H. M. Kasper

F. HIGH-PRESSURE FORMS OF $CsNiF_3$

It was reported previously[17] that at high pressure (about 65 kbars) $CsNiF_3$ is transformed into a hexagonal close-packed structure isomorphous with $CsMnF_3$ (Ref. 18). A more extensive study of the pressure-temperature phase diagram of $CsNiF_3$ has revealed the existence of a second high-pressure phase. The results of this study, which were obtained by x-ray diffraction measurements on samples annealed at pressures up to 65 kbars and temperatures between

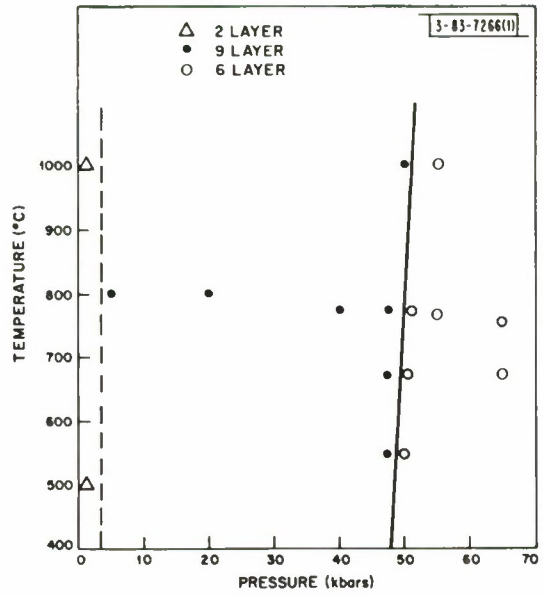

Fig. III-12. Pressure-temperoture phose diagrom for $CsNiF_3$.

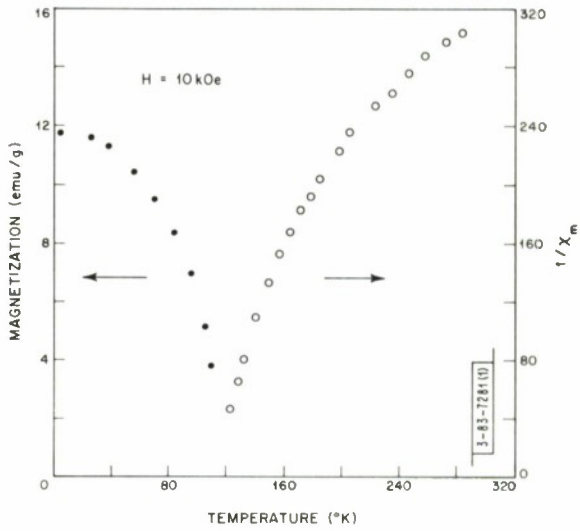

Fig. III-13. Mognetizotion ond reciprocol mognetic susceptibility vs temperoture for $CsNiF_3$ (6L).

500° and 1000°C, are summarized by Fig. III-12. The hexagonal two-layer structure (2L) stable at atmospheric pressure[19] transforms at less than 5 kbars to the hexagonal nine-layer structure (9L). This stacking sequence has a large field of stability, which extends to about 50 kbars. The pressure of the transformation from 9L to the 6L form is essentially temperature independent.

The pressure-induced transformations are accompanied by rather large changes in volume. The 2L to 9L phase change results in a 9-percent decrease in volume, while the 9L to 6L transformation shows a 4-percent decrease. These volume changes are calculated from the following lattice constants determined at atmospheric pressure: 9L, a = 6.12 Å, c = 22.15 Å; and 6L, a = 6.05 Å, c = 14.54 Å.

The magnetic properties of the high-pressure forms of $CsNiF_3$ were studied by making magnetic susceptibility measurements from 4.2° to 300°K in fields to 17.2 kOe with a vibrating-sample magnetometer.

At temperatures greater than 80°K, the susceptibility of the 9L modification obeys the Curie-Weiss law with $\mu_{eff} = 3.2\,\mu_B$ and a $\Theta_p = -75$°K. There appeared to be a trace amount of ferromagnetic impurity with a T_c between 70° and 80°K, as indicated by the variable magnitude of a susceptibility discontinuity in this interval. Also, different samples showed varying amounts of saturation effects in the field studies at 4.2°K. The μ_{cff} for this 9L form corresponds to that for a Ni^{2+} ion with g = 2.3.

The 6L modification exhibits a ferrimagnetic transition (Fig. III-13) with $T_c = 111$°K as determined from the inflection point in the susceptibility measured at $H_a = 500$ Oe. This T_c is similar to those reported for the isostructural compounds $RbNiF_3$ ($T_c = 139$°K) (Ref. 20) and $TlNiF_3$ ($T_c = 150$°K) (Ref. 21). The saturation moment for $CsNiF_3$ found at 4.2°K and 17.2 kOe is $0.6\,\mu_B$/Ni. This is lower than the predicted value of $0.77\,\mu_B$/Ni for a ferrimagnet with only one-third of the Ni spins (g = 2.3) uncompensated, as described for $RbNiF_3$ (Ref. 20). The

reduction in σ_s is probably due to the very high anisotropy observed for this hexagonal structure, for which applied fields greater than 50 kOe are required to achieve saturation.

The change in T_c with hydrostatic pressure to 8 kbars, as determined in a vibrating-coil magnetometer,[22] corresponds to $dT_c/dP = +0.53$ deg/kbar. For $RbNiF_3$, $dT_c/dP = +0.60$ deg/kbar. With localized d electrons at Ni^{2+} ions having the configuration $t_{2g}^6 e_g^2$, only Ni-F-Ni interactions are possible and a $dT_c/dP > 0$ is compatible with superexchange theory.[23]

TABLE III-3

OPTICAL ABSORPTION OF Ni^{2+} ($3d^8$) IN $RbNiF_3$ AND $CsNiF_3$

	Absorption Peaks (μm)		
Term	Free Ion	$RbNiF_3$ (6L)	$CsNiF_3$ (6L)
$^3A_{2g}$	Ground state	Ground state	Ground state
$^3T_{2g}$	1.16	1.41	1.53
^1E_g	0.745	0.760	0.776
$^3T_{1g}$	0.675	0.668	0.644
$^1T_{2g}$	0.460	0.496	0.512
$^3T_{1g}$	0.410	0.480	0.476
$^1A_{1g}$	0.385	0.428	0.438
^1E_g	0.355	0.330	–
$^1T_{2g}$	0.280	0.280	–

Optical transmission measurements with double-beam spectrometers in the range 0.2 to 15 μm were made on polycrystalline $CsNiF_3$ (6L) hot pressed into KBr disks or suspended in index-matching liquids. All of the known Ni^{2+} (d^8) transitions were observed. (Table III-3 compares the optical data for $CsNiF_3$ (6L) and $RbNiF_3$.) Of practical interest, the $^3T_{1g}$ transition in $CsNiF_3$ (6L) occurs at 0.476 μm, which is an extremely good match for Kr and Ar CW lasers. Lattice absorption begins at 7 μm in $RbNiF_3$, while the long wavelength edge in $CsNiF_3$ (6L) has shifted to 9 μm.

J. M. Longo
J. A. Kafalas
J. R. O'Connor
D. A. Batson
T. W. Hilton

G. STRUCTURAL, ELECTRICAL, AND MAGNETIC PROPERTIES OF HIGH-PRESSURE $CdCr_2Se_4$

At high pressures and temperatures, $CdCr_2Se_4$ is transformed from the cubic spinel structure to a defect NiAs structure with monoclinic symmetry. The boundary between the two phases at temperatures between 400° and 750°C was reported previously.[24] Linear extrapolation of this boundary to room temperature gives a transformation pressure of about 70 kbars. In order to check this value, measurements have been made with two diamond-anvil high-pressure x-ray diffraction units.[25] Experiments with the first unit, which is pressurized by means of N_2 gas, showed that the transformation does not take place at pressures up to about 80 kbars, the maximum pressure this apparatus can attain. With the second unit, which is screw loaded and cannot be calibrated as accurately, the pure monoclinic phase was obtained at pressures estimated to exceed 100 kbars. These results indicate that at room temperature the transformation occurs between about 80 and 100 kbars, and therefore that the phase boundary exhibits appreciable curvature below 400°C. From the data obtained for the lattice parameter of the spinel phase as a function of pressure, it is found that the compressibility $(-\Delta V/V_o)$ for this phase is relatively small and decreases with pressure, from 6×10^{-4} kbar^{-1} between 1 atm and 35 kbars to 3×10^{-4} kbar^{-1} between 35 and 65 kbars.

Earlier x-ray diffraction data on samples of the high-pressure phase retained at atmospheric pressure showed that this phase has monoclinic symmetry.[24] A lattice parameter determination has now been made on the basis of additional diffraction patterns obtained for retained samples. Initially, attempts were made to index the patterns according to the structure of the high-pressure phases of $FeCr_2S_4$ and $MnCr_2S_4$ (Ref. 26). This structure is derived from that of Cr_3S_4 (Ref. 27), which may also be designated as $CrCr_2S_4$, since it contains both Cr^{+2} and Cr^{+3} ions. Although a reasonably good fit was obtained, the theoretical density was nearly 20 percent higher than the measured density. A better fit, particularly for the low-angle diffraction lines, is obtained for a unit cell similar to that of $CrCr_2S_4$, but with the a and b parameters approximately doubled. The best values for the monoclinic cell parameters are: a = 14.62 Å, b = 6.90 Å, c = 11.45 Å, and $\beta = 90.5°$. The theoretical density is 6.1 g/cm^3, in fair agreement with the measured value of 5.8 g/cm^3.

Electrical measurements were made on crack-free samples obtained from cylindrical ingots of both monoclinic and spinel phases. The samples are p-type, with resistivities at room temperature ranging from 3.2 ohm-cm to 22×10^{-2} ohm-cm for the monoclinic phase, and from 1.7 ohm-cm to 5×10^3 ohm-cm for the spinel phase. A resistivity range of about six orders of magnitude has been reported for p-type spinel samples, depending on impurity concentration.[28] Data for representative samples of each phase obtained from the same batch of material are given in Table III-4. The electrical properties of the monoclinic phase do not show whether it is a semimetal or a degenerate semiconductor. The resistivities of the monoclinic samples are about an order of magnitude higher than those for the monoclinic thiospinels, and the temperature coefficient of resistivity is much lower than for the thiocompounds. The Seebeck coefficients of the two $CdCr_2Se_4$ phases are of the same magnitude as those for $NiCr_2Se_4$ and $CrCr_2Se_4$ (Ref. 29).

The monoclinic phase of $CdCr_2Se_4$ orders antiferromagnetically, with a Néel point of 55°K, and has a very small magnetic moment ($0.035\ \mu_B$) at 4.2°K. Thus, its magnetic properties are completely different from those of the spinel phase, which is ferromagnetic (Curie point 135°K)[30]

TABLE III-4
ELECTRICAL PROPERTIES OF $CdCr_2Se_4$

	Spinel		Monoclinic	
	300°K	77°K	300°K	77°K
Resistivity (ohm-cm)	1.8	1.6	6.8×10^{-2}	4.6×10^{-2}
Holl coefficient (cm^3/C)	2.75	1.33	2.2×10^{-2}	2.6×10^{-2}
Corrier concentration (cm^{-3})	2.3×10^{18}	4.7×10^{18}	2.9×10^{20}	2.5×10^{20}
Hall mobility ($cm^2/V\text{-sec}$)	1.6	0.82	0.32	0.56
Seebeck coefficient ($\mu V/deg$)	44	–	61	–

and has a magnetic moment of $5.55\,\mu_B$ at 4.2°K. The temperature dependence of the magnetic susceptibility for a sample of the monoclinic phase is shown in Fig. III-14, where the location of the Néel point is obvious. The susceptibility of this sample, which did not contain any of the spinel phase, was found to vary linearly with magnetic field between 0 and 17 kOe at 4.2°, 77°, and 295°K, as expected for antiferromagnetic or paramagnetic materials. The data for 77°K are shown by the lower curve in Fig. III-15.

The magnetic properties of monoclinic samples are strongly affected by the presence of small quantities of the ferromagnetic spinel phase. This effect is illustrated by the upper curve of Fig. III-15, which gives the field dependence of the susceptibility at 77°K for a sample containing 5- to 10-percent spinel. (This sample was prepared by heating the pure monoclinic sample of the lower curve at 125°C for 35 hours.) The relative susceptibility increases rapidly at

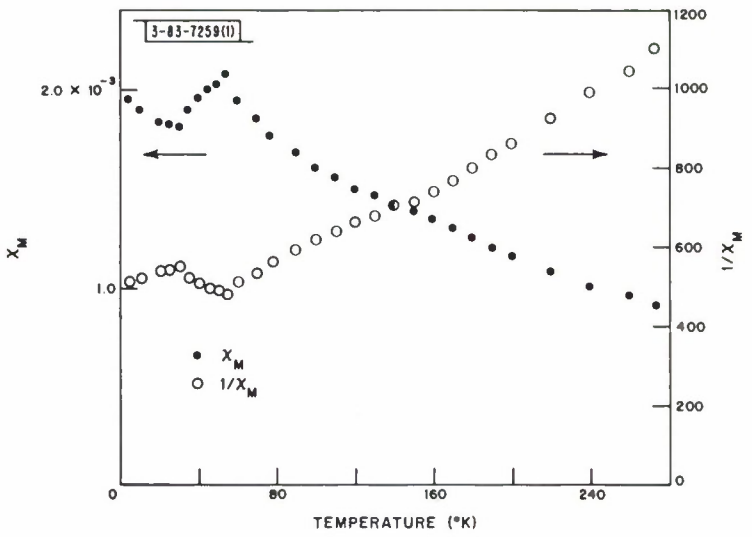

Fig. III-14. Magnetic susceptibility and reciprocal susceptibility vs temperature for high-pressure monoclinic phase of $CdCr_2Se_4$.

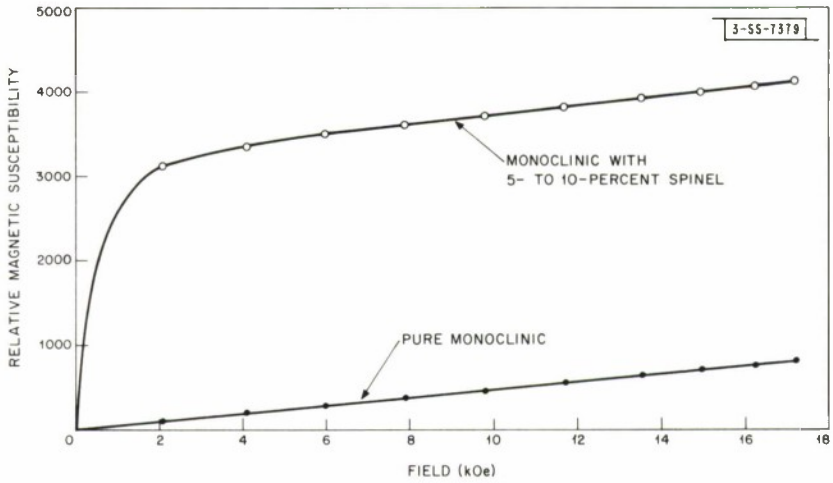

Fig. III-15. Mognetic susceptibility os o function of mognetic field for two samples of $CdCr_2Se_4$.

low fields and then saturates, due to the spinel phase, after which it increases slowly in the same manner as for the pure monoclinic sample. The curve of susceptibility vs temperature for the mixed sample exhibits anomalies at both 55° and 135°K, corresponding to the Néel point of the monoclinic phase and the Curie point of the spinel phase. In samples containing sufficient spinel phase, the Néel point is partially or completely obscured.

Some samples of the monoclinic phase have been found to contain traces of Cr_2Se_3 (Ref. 24), which has a Néel point of about 25°K. A sample prepared by mixing 5-percent Cr_2Se_3 with the pure monoclinic phase exhibited two Néel temperatures: one at ~25°, and the other at ~55°K. This shows that the antiferromagnetic ordering observed in monoclinic samples is not due to the presence of Cr_2Se_3.

The observation of antiferromagnetic ordering in the monoclinic phase of $CdCr_2Se_4$ shows that this phase behaves magnetically in the same manner as the monoclinic sulfides MCr_2S_4, where M is Mn, Fe, Co, or Ni, although the antiferromagnetic ordering temperature (55°K) is much lower than those for the sulfur compounds.[31] The low magnetic moment and antiferromagnetic ordering for $CdCr_2Se_4$ could be explained in two ways. The defect-NiAs structure is the result of ordering of divalent ions (Cd^{++}) and vacancies on planes between the planes of trivalent ions (Cr^{+++}).[32] Therefore, the alternate planes of Cr ions could have their magnetic vectors opposed, as suggested by Bertaut, et al.,[33] for Cr_3S_4 and Cr_3Se_4. On the other hand, alternate Cr^{+++} ions within each plane $(10\bar{1})$ could have their spins aligned in opposition so that the overall structure has antiferromagnetic behavior.

M. D. Banus
M. C. Lavine

REFERENCES

1. A. Glassner, "The Thermochemical Properties of the Oxides, Fluorides, and Chlorides to 2500°K," ANL-5750, Argonne National Laboratory.
2. J. Steininger and R. E. England, Trans. Met. Soc. AIME 242, 444 (1968).
3. B. M. Kulwicki, Ph. D. Thesis, Department of Chemical Engineering, University of Michigan (1963).
4. J. Carides and A. G. Fischer, Solid State Commun. 2, 217 (1964).
5. M. R. Lorenz, J. Phys. Chem. Solids 23, 939 (1962).
6. A. J. Strauss, personal communication.
7. A. Reisman, M. Berkenblit, and M. Witzen, J. Phys. Chem. 66, 2210 (1962).
8. A. J. Strauss and L. B. Farrell, J. Inorg. Nucl. Chem. 24, 1211 (1962).
9. F. E. Karasz and J. M. O'Reilly, Rev. Sci. Instr. 37, 255 (1966).
10. T. Ashworth and H. Steeple, Cryogenics 8, 225 (1968).
11. D. J. David, Anal. Chem. 36, 2162 (1964).
12. J. N. Bierly, L. Muldawer, and O. Beckman, Acta Met. 11, 447 (1963).
13. W. H. Grodkiewicz, E. F. Dearborn, and L. G. Van Uitert, in Crystal Growth, edited by H. S. Peiser (Pergamon Press, Oxford, England, 1967), p. 441.
14. A. Ferretti, W. Kunnmann, and A. Wold, J. Appl. Phys. 34, 388 (1963).
15. A. Magneli, Arkiv. Kemi. Min. Geol. 15B, No. 3 (1941)
16. J. B. Taylor and R. D. Heyding, Can. J. Chem. 36, 597 (1958).
17. Solid State Research Report, Lincoln Laboratory, M. I. T. (1968:3), p. 31.
18. A. Zalkin, K. Lee, and D. Templeton, J. Chem. Phys. 37, 697 (1962).
19. D. Babel, Z. Naturforsch. 20a, 165 (1965).
20. M. W. Shafer, T. R. McGuire, B. E. Argyle, and G. J. Fan, Appl. Phys. Letters 10, 202 (1967).
21. K. Kohn, R. Fukuda, and S. Iida, J. Phys. Soc. Japan 22, 333 (1967).
22. N. Menyuk, J. A. Kafalas, K. Dwight, and J. B. Goodenough, J. Appl. Phys. (to be published).
23. J. B. Goodenough, Phys. Rev. 164, 785 (1967), DDC 668715.
24. Solid State Research Report, Lincoln Laboratory, M. I. T. (1968:3), p. 28.
25. M. D. Banus and M. C. Finn, J. Electrochem. Soc. (to be published).
26. R. J. Bouchard, Materials Res. Bull. 2, 459 (1967).
27. M. Chevreton and F. Bertaut, Compt. Rend. 253, 145 (1961).
28. H. W. Lehmann and G. Harbeke, J. Appl. Phys. 38, 946 (1967).
29. R. J. Bouchard and A. Wold, J. Phys. Chem. Solids 27, 591 (1966).
30. "Bibliography of Magnetic Materials and Tabulation of Magnetic Transition Temperatures," ORNL-RMIC-7, Oak Ridge National Laboratory, Oak Ridge, Tennessee (March 1968), p. 3.
31. R. E. Tressler and V. S. Stubican, J. Am. Ceram. Soc. 51, 391 (1968).
32. G. Berodias and M. Chevreton, Compt. Rend. 261, 2202 (1965).
33. F. Bertaut, G. Rault, R. Aléonard, R. Pauthenet, N. Chevreton, and R. Jansen, J. Phys. (Paris) 25, 582 (1966).

IV. PHYSICS OF SOLIDS

A. ELECTRONIC BAND STRUCTURE AND ELECTRONIC PROPERTIES

1. Magneto-optical Investigation of Bi-Sb Alloys†

The study by oscillatory magnetoreflection of the band structure at the L point in Bi-Sb alloys has continued. Figure IV-1 gives a summary of the data for the 8-percent alloy. Corresponding data have been obtained also for Bi-Sb alloys‡ of 0-, 3-, 12-, and 15-percent antimony. These results have been analyzed in terms of the Lax two-band model to obtain effective masses, energy gaps, and momentum matrix elements. The variation of these parameters with alloying is plotted in Fig. IV-2. Surprisingly, not only the effective mass and energy gap but also the momentum matrix element varies with antimony content.

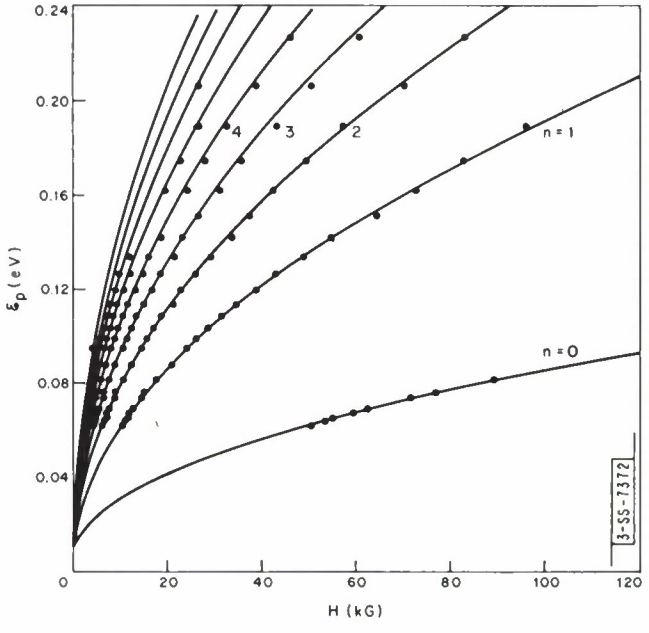

Fig. IV-1. Summary of Bi-Sb magnetoreflectian results for an 8-percent antimony alloy.

Results such as those of Fig. IV-2 indicate that the energy gap goes to zero at a composition of ~2-percent antimony and that near this composition the alloy also becomes semiconducting. This latter conclusion is also substantiated by the temperature dependence of the energy gap and the plasma edge. The fact that our measured temperature coefficient of the energy gap, $\delta_{L_s} - \delta_{L_a}$, of the semimetal bismuth has a sign opposite that of the semiconducting alloys suggests that the bonding and antibonding bands (L_s and L_a, respectively) invert after they cross.

† This experiment was carried out using the high field facilities of the Francis Bitter National Magnet Laboratory, M.I.T.

‡ We are grateful to Dr. W. M. Yim of RCA for supplying us with these alloys.

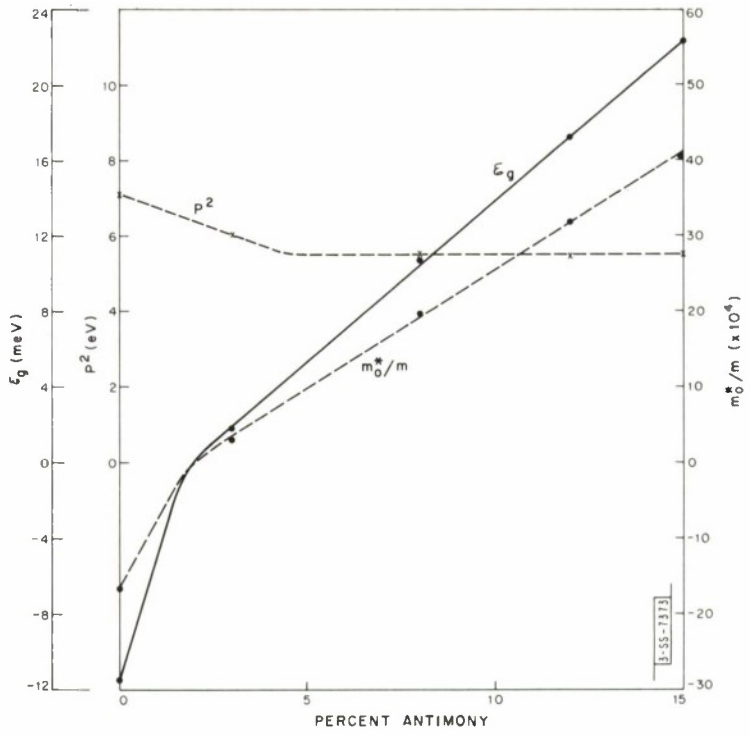

Fig. IV-2. Voriotion in Bi-Sb olloys of energy gop $\mathcal{E}_g$ ($= \mathcal{E}_{L_s} - \mathcal{E}_{L_o}$), reduced effective moss ot bottom of bond m_o^*, ond momentum motrix element P. T ~ 4°K.

These effects can be understood in terms of the change in the magnitude of the spin-orbit splitting with alloying. Since the lattice constants of bismuth and antimony are nearly equal (e.g., c = 11.86 Å for bismuth and 11.27 Å for antimony), the crystal field, as suggested by Mase,[1] is probably not modified much by alloying. The largest change in the crystal field should be the decrease in the average spin-orbit interaction energy as antimony is added to bismuth. On this assumption, our preliminary calculations predict semiquantitatively the measured energy gap variation with alloying, and also the band inversion.

E. Tichovolsky†
J. G. Mavroides
D. F. Kolesar

2. Shubnikov-de Haas Studies in $Pb_{1-x}Sn_xTe$‡

The Shubnikov-de Haas effect is being used to investigate the band structure of PbTe-SnTe alloys. Measurements of the periods and amplitudes of the oscillations were carried out in 17-, 20-, and 30-percent tin alloys in the temperature range 1.25° to 4.2°K with magnetic fields up to 80 kG. The results for p-type $Pb_{1-x}Sn_xTe$ are summarized in Table IV-1.

† Department of Physics, M.I.T.

‡ This experiment was carried out using the high field facilities of the Francis Bitter National Magnet Laboratory, M.I.T.

TABLE IV-1

SUMMARY OF VALUES OF PARAMETERS IN p-TYPE $Pb_{1-x}Sn_xTe$

Campositian: x $Pb_{1-x}Sn_xTe$	Carrier Concentratian (cm^{-3})	m_t/m	K	$g_{\|\|}$	$g_{\perp}$
0.17	0.7×10^{18}	0.022	11.5	–	–
0.20	1.1×10^{18}	0.022	10	29	9

In the abave, m_t is the transverse effective mass, K is the ratia af langitudinol ta transverse effective moss, ond $g_{||}$ ond $g_{\perp}$ are the longitudinal and transverse g-factors with respect to the (111) direction.

J. Melngailis J. G. Mavroides
W. C. Kernan J. O. Dimmock
T. C. Harman

3. Transport Equation for an Impure Nearly Degenerate Fermi System to All Orders in Impurity and Interparticle Interaction

The problem of transport in an impure normal Fermi system has been studied. A quasi-particle transport equation has been derived for this system subject to the limitations of low temperatures, small impurity densities and slowly varying driving fields.

The calculations involved have been carried out by the use of temperature Green's function techniques to all orders in the interfermion and impurity interaction strengths, and to first order in the impurity density. It should be stressed that this work represents an important advance over a previously reported calculation[2] which, by a different method, was carried out only to finite order. In this work, essential use was made of the analytic properties of the one- and two-particle Green's functions.

The quasi-particle distribution function, which has been shown to be related to the induced current and particle densities in a way identical to that proposed by Landau[3] for a pure system at zero temperature, satisfies an equation which is similar to the Landau equation but with impurity and interparticle scattering terms added. The problem of the long range of the Coulomb potential is easily handled so that the theory can be applied to normal metals.

Details of this work will appear in a future publication.

J. L. Sigel

4. Symmetry of the Ground Level of a Hamiltonian

An investigation has been made concerning what can be said from general considerations about the symmetry of the ground state of a system. For example, can one determine without calculation (a) that the ground energy level of a two-electron one-center system (such as the H^- ion or the He atom) must have S_g symmetry, and (b) that the ground level of a two-electron

homonuclear diatomic molecule must have Σ_g^+ symmetry? We find, on the basis of a general relation between nodelessness and symmetry of a wave function, that the answer is, in fact, yes for these and other systems. We prove that a real nodeless energy eigenfunction with energy E has a nonzero part which also is an eigenfunction with energy E and which, under coordinate transformations, has the full symmetry of the Hamiltonian. This result can be applied to many systems of physical interest for which the ground state energy eigenfunction is known from the nature of the Hamiltonian to be nodeless. (In particular, this is true for the specific systems mentioned above.) However, we have found simple counterexamples showing that not all Hamiltonians have a nodeless ground state energy eigenfunction. A report of this investigation will appear in the Journal of Mathematical Physics.

W. H. Kleiner
T. A. Kaplan

B. MAGNETISM

Sections 1 through 3 below are Abstracts of papers to be presented at the Annual Conference on Magnetism and Magnetic Materials, New York, 18 to 21 November 1968.

1. "Pressure Effect Measurements Using a Vibrating-Coil Magnetometer

"A vibrating-coil magnetometer used in conjunction with a helium-gas pressure-generating system has proved to be a versatile new means of studying the effects of hydrostatic pressure on magnetic properties. The sensitivity of this system permits the measurement of paramagnetic susceptibilities on powder samples of the order of 0.1 grams.

"Paramagnetic measurements on MnAs, which undergoes a hexagonal-orthorhombic transition upon application of pressure, have directly established that the transition is accompanied by a change of the manganese ions from a high-spin to a low-spin state. Regions in the pressure-temperature space in which the high-pressure (orthorhombic) phase is metamagnetic and ferromagnetic have been delineated.

"In addition, the pressure dependence of the magnetic-ordering transition temperature has been determined for a number of materials, and the results are consistent with the predictions of Goodenough where applicable. Finally, it has been established that this instrument can be used to study the effect of pressure on magnetic anisotropy."

N. Menyuk K. Dwight
J. A. Kafalas J. B. Goodenough

2. "Distant-Neighbor B-B Interactions in Cobalt Chromite

"We have recently shown that five distinct distant-neighbor B-B exchange interactions can play significant roles in determining the ground-state spin configuration in chromium spinels having non-magnetic A-site ions. This investigation is now extended to the case of magnetic A-site ions and to include A-A interactions, and the results are used to reinterpret our experimental findings for cobalt chromite.

"Reasonable values for the distant-neighbor interactions lead to an eight percent decrease in the theoretical wavelength of the minimum-energy ferrimagnetic spiral, which brings it into agreement with the observed value. Furthermore, inclusion of these values in the minimization of the free energy (in the molecular-field approximation) leads to the prediction of an additional magnetic transition (where a phase angle vanishes) at about one third of T_c. The resulting kink in the computed variation of magnetization with temperature is in close agreement with experiment. Our neutron diffraction pattern is shown to be incompatible with contradictory results recently reported for a $CoCr_2O_4$ sample produced by conventional ceramic techniques. The overall agreement between theory and experimental results obtained with our sample indicates that the precursor method of preparation yields more nearly ideal $CoCr_2O_4$."

K. Dwight
N. Menyuk

3. "Some Applications of the Thermal Single-Determinant Approximation

"A new generalization of Hartree-Fock (HF) theory to non-zero temperature, T, namely the Thermal Single-Determinant Approximation (based on the variational principle of statistical mechanics) has been applied to two systems, (a) a homogeneous interacting fermion gas, and (b) a crystal of widely separated hydrogen atoms treated in a limited configuration-interaction model. (a) For the fermion gas, a plane wave solution is found, and shown to yield identical thermodynamic behavior to the plane wave solution of the standard thermal HF approximation (STHFA). (b) For the H-atoms, the new theory gives a lower free energy than the STHFA. It is shown that, in addition, the new theory requires the one-electron functions ψ_i to be localized for the case of the weakly interacting atoms, whereas the STHFA for the same case apparently requires the ψ_i to be extended through the crystal. As far as we know, this is the first variational derivation in which one-electron states in a crystal must be localized."

T. A. Kaplan
P. N. Argyres

4. Spherical Model as the Limit of Infinite Spin Dimensionality

Consider the Hamiltonian $H = -J \sum_{ij} S_i \cdot S_j$, where S_i are isotropically interacting D-dimensional classical spins. For D = 1, 2, and 3, this reduces to the $S = \frac{1}{2}$ Ising, classical planar, and classical Heisenberg models, respectively. It has recently been proved formally[4] that as $D \to \infty$, H reduces to the exactly soluble spherical model of Berlin and Kac (BK).[5] Here, we remark at greater length upon why our result has proved to be of some utility.

(a) A knowledge of the properties of H in the limit $D \to \infty$, provides one with an "anchor point," since H is not soluble for other values of D (except for the linear chain lattice – and for 2-dimensional lattices, provided that D = 1). We have calculated 100 terms in the various expansions (specific heat, susceptibility, ...) for the spherical model. The fact that the "correct" values for the various critical properties are indicated (by standard

extrapolation procedures) serves as a useful piece of evidence against frequently made assertions that the regularity observed in the first ten or so terms of the expansions available for general D are misleading or spurious.

(b) BK[5] pointed out that the free energy of the spherical model could be expressed in exactly the same "form" as the free energy of the Ising model for 1- and 2-dimensional lattices [cf. BK, Eq. (47) with BK, Eq. (9)]. Thus, they were led to conjecture the (as yet unknown) form of the Ising model free energy for 3-dimensional lattices [BK, Eq. (48)]. We have noted that for the 1-dimensional lattice, the free energy has in fact the same form for all D as it has for D = 1 and ∞; hence, we are led to conjecture, in much the same spirit as BK, that the general form of the free energy $\psi(D, d)$ for arbitrary D and for arbitrary d-dimensional hypercubical lattices is

$$\beta\psi(D, d) \propto \pi^{-d} \int_0^\pi \cdots \int_0^\pi d\omega_1 \cdots d\omega_d \ln\left[F(D, d, T) - G(D, d, T) \sum_{m=1}^{d} \cos\omega_m\right] \qquad \text{(IV-1)}$$

where F(D, d, T) and G(D, d, T) are unknown functions of D, d, and temperature T.

H. E. Stanley

C. SCATTERING EXPERIMENTS WITH LASERS

1. Light Scattering Study of Anharmonic Interactions in α-Quartz

The temperature dependences of the damping of two optic vibrations (the 128-cm^{-1} E-mode, and the 466-cm^{-1} A_1-mode) and a longitudinal acoustic vibration along the x-axis have been measured by high-resolution Raman and Brillouin scattering in α-quartz. The 128-cm^{-1} mode is the lowest-lying optical vibration in quartz and shows a marked increase in lifetime at low temperatures. Utilizing available phonon dispersion data obtained by neutron spectroscopy, the linewidth and shift are calculated in terms of three phonon interactions. Such a calculation is depicted in Fig. IV-3 where it is applied to the 128-cm^{-1} mode width. A simple model for the

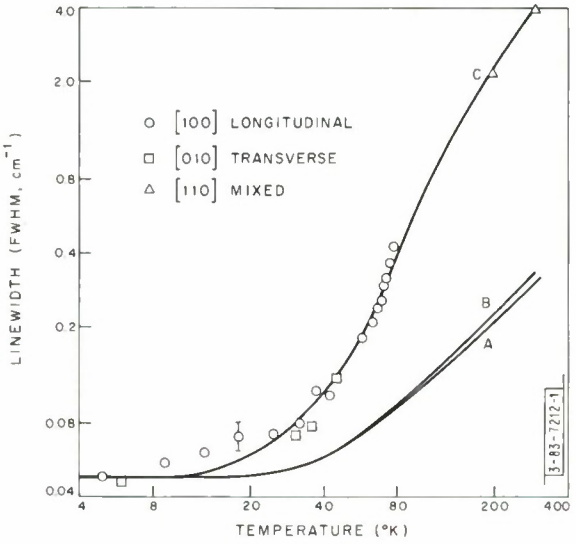

Fig. IV-3. Linewidth of 128-cm^{-1} E-mode in α-quartz as function of temperature. Points are experimental, and curves are theoretical. Curve A: decay into two sharp acoustic modes only; curve B: decay into two relaxation broadened acoustic modes only; curve C: decay into acoustic modes and scattering of thermal phonons.

cubic anharmonicity, which includes relaxation broadening of the thermal phonons, accounts satisfactorily for the residual damping at low temperatures.

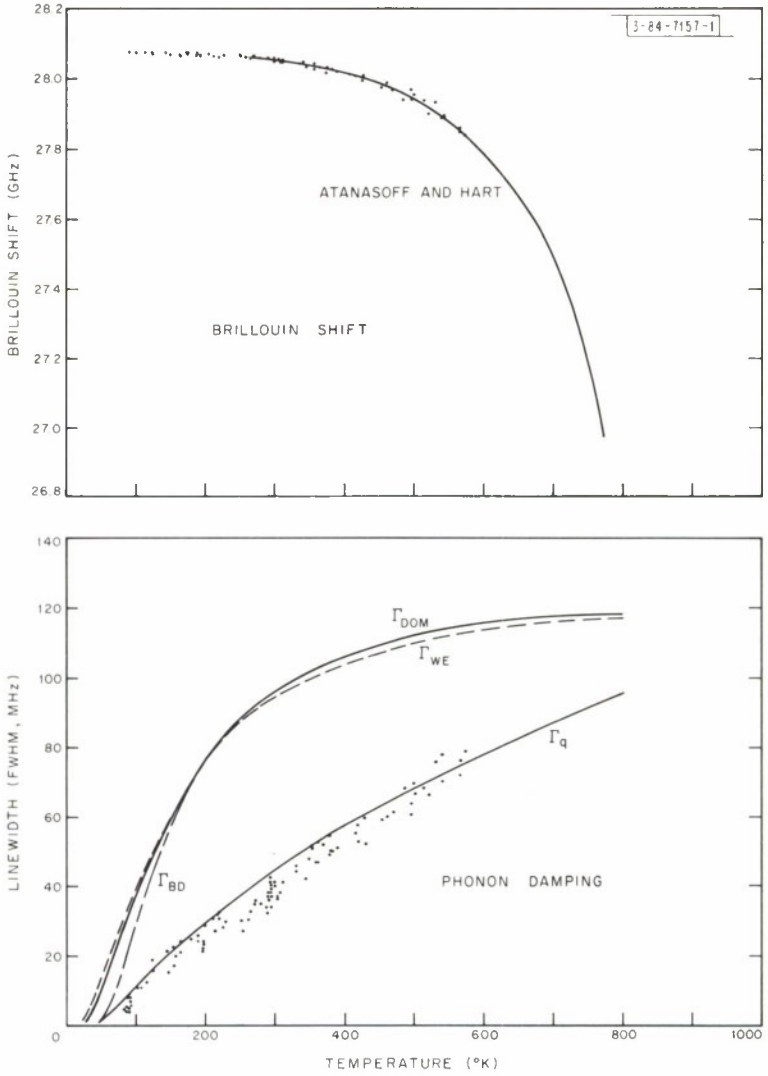

Fig. IV-4. Shift and width af 28-GHz langitudinal acaustic phanans alang x-axis af α-quartz. Paints are experimental, and curves are thearetical. Γ_{DOM}, Γ_{WE}, and Γ_{BD} represent variaus single-relaxatian time theories, and Γ_q represents a distributed relaxatian pracess.

Velocity and attenuation of the acoustic wave at a frequency of 28 GHz are measured from the Brillouin shift and linewidth as given in Fig. IV-4. Standard "single-relaxation time" theories do not adequately explain the linewidth behavior, so the data are fit with a distributed relaxation process.

A. S. Pine

2. Raman Scattering by Magnetic Excitations in $RbNiF_3$

An investigation of Raman scattering of argon laser light (λ = 5145 Å) from the hexagonal ferrimagnet $RbNiF_3$ (Ref. 6) revealed at T ≅ 15°K an intense, broad symmetrical line shifted ~510 cm^{-1} from the laser excitation energy. At higher temperatures as its amplitude decreased, the line broadened and its shift decreased. It was still intense at the Curie temperature (139°K), and remained observable to temperatures near 200°K. This line, assumed to arise from magnetic excitations, is best described in the ordered state as due to scattering from two magnons near the Brillouin zone edge, and at T_c and above as due to scattering from a cluster.

$RbNiF_3$ has a hexagonal structure D_{6h}^4 with easy plane anisotropy. Each Ni^{2+} ion is in an octahedron of F^- ions, with two-thirds of these octahedra (each containing a B-site Ni^{2+} ion) sharing one common face and one-third (each containing an A-site Ni^{2+} ion) sharing only corners. The important interactions are assumed to be between nearest-neighbor B ions (with ferromagnetic $J_{BB'} < 0$), nearest-neighbor A and B ions (with antiferromagnetic $J_{AB} > 0$), and several second-neighbor interactions, roughly equal (with small antiferromagnetic $J_{AA} > 0$). The ground state is taken to be the collinear Néel state with A and B spins antiparallel.[7,8]

Neglecting anisotropy, we have calculated the spin wave spectrum of $RbNiF_3$ in the linear approximation. From optical absorption data in $RbNiF_3$ (Ref. 9), we identify the two modes responsible for causing magnon sidebands in absorption. The combination of these modes, occurring near the Brillouin zone edge and having zero net wave vector, is presumed to cause the observed Raman scattering. Using an additional susceptibility measurement,[7] we obtain the following values for the dominant exchange interactions: $J_{BB'} = -113\,cm^{-1}$, $J_{AB} = 48\,cm^{-1}$, and $J_{AA} = 4\,cm^{-1}$.

From these derived exchange constants, we have calculated the Curie temperature and the temperature at which the A sublattice reverses its magnetization in an applied field. The results of a normal molecular field calculation and a modified molecular field calculation with a two-spin cluster were compared with experimental results.[8] The calculated temperatures were high in both cases, with better agreement for the modified molecular field treatment.

Above the Curie temperature, the temperature dependence of the Raman shift is related to the energy of a spin-flip transition within a localized cluster. The Raman shift then gives a qualitative estimate of the short range order, or nearest-neighbor spin correlation function, for those spins involved in the spin-flip transition.

Work is now under way on a more accurate calculation of T_c from the exchange constants, using the Bethe-Peierls-Weiss method. Also, we are investigating the selection rules for magnon scattering and a more quantitative relation between the Raman shift and spin correlation function.

S. R. Chinn
H. J. Zeiger

3. Light Scattering from InAs and InSb Surfaces

We have studied Raman scattering from zone center optic phonons in InAs and InSb at temperatures from 5° to 300°K by a surface reflection technique using an argon-ion laser. Enhancement of the LO phonon intensity was observed when the laser frequency lay near an interband transition, an effect similar to that recently reported.[10] In InSb at 10°K, the LO phonon intensity relative to the TO phonon increased by over an order of magnitude as the laser wavelength was increased from 4765 to 5145 Å, hence approaching the interband transition $E_1 + \Delta_1$

(2.38 eV at 300°K). A significant enhancement (factor of 3) of the LO scattering intensity relative to the TO was also observed in InAs as the laser frequency approached the E_1 gap (2.505 eV at 300°K). Using the 4880-Å line (2.54 eV), we observed the LO phonon intensity when the InAs surface was biased with an electric field using an electrolytic cell.[11] The external field produced a significant enhancement of the scattering amplitude (>50 percent), and the LO scattering frequency decreased 5 cm^{-1} at the highest field. The TO phonon was unaffected. Using this large electric field effect, we have synchronously detected the LO scattering at the electric field modulation frequency. Our results are interpreted in terms of the surface electric field which produces a change in the dielectric constant through the electro-optic coefficient.

K. W. Nill
A. Mooradian

4. Raman Scattering from Spin-Density Fluctuations in n-GaAs (Abstract of paper presented at International Conference on Light Scattering Spectra of Solids, New York University, 3-6 September 1968)

"The anomalously large cross sections observed for scattering from single-electron excitations in GaAs can be explained in part as scattering from spin-density fluctuations. The electromagnetic field is coupled to the spins through second-order $\mathbf{p} \cdot \mathbf{A}$ perturbation terms involving the spin-orbit splitting of the valence band. At high carrier densities, where the screening wave vector is much greater than the momentum transfer, the spin-density fluctuations are not screened out as the charge-density fluctuations are, and hence the cross section can be much larger than that due to charge-density fluctuations alone. The polarization properties of the scattered radiation are also different for the two processes. For spin-density scattering the matrix element is proportional to $\vec{\sigma} \cdot (\hat{\epsilon}_1 \times \hat{\epsilon}_2)$, whereas for charge-density scattering it varies as $(\hat{\epsilon}_1 \cdot \hat{\epsilon}_2)$, where $\hat{\epsilon}_1$ and $\hat{\epsilon}_2$ are the incident and scattered polarization vectors. The magnetic field is taken to be zero throughout."

D. C. Hamilton
A. L. McWhorter

5. Magneto-Raman Scattering with $\Delta n = 1$, $\Delta s = 0$

An experimental investigation of magneto-Raman scattering on n-type InSb by Slusher, Patel and Fleury[12-14] confirmed several scattering processes which had been predicted theoretically,[15-17] but also demonstrated that there was a process which had not been predicted in which $\Delta n = 1$, $\Delta s = 0$, i.e., a process in which an electron changes its Landau level number by one with no change in spin state. Two single-electron mechanisms were proposed to explain this process: the first uses the linear-k inversion asymmetry terms which are present in the energy E(k) of the InSb valence band; the other uses the interactions between Landau levels which occur off $k_3 = 0$, where k_3 is along the direction of the magnetic field. Recently, two estimates of the cross section for the $k_3 \neq 0$ mechanism were made and agreement with the experimental cross section was claimed.[18,19] However, we have studied both of the mechanisms in detail and find that the predicted cross sections are several orders of magnitude smaller than those observed experimentally. This suggests that other mechanisms, such as Coulomb interactions, are

important. These conclusions have been presented recently.[20] The details of our evaluation have been written in a separate report.[21] A brief description of our work and our objections to the estimates of Refs. 18 and 19 are given below.

The treatment of Luttinger[22] for the magnetic energy levels of the valence bands and that of Pidgeon and Brown[23] which includes the conduction band as well show that to a good approximation there is a decoupling of the magnetic Hamiltonian in two parts. As a result, the wavefunctions fall into two sets (commonly denoted as the A and B sets), and there is no admixing between sets. For example, in the treatment of Ref. 23, the A and B sets each contain one conduction band Landau level ladder, a heavy hole ladder, a light hole ladder and a split-off band ladder. For interband magneto-optical transitions, only A and A or B and B states connect in the Faraday configuration, while in the Voigt configuration only A and B states connect. From this decoupled scheme, all the observed magneto-Raman scattering processes are predicted except the $\Delta n = 1$, $\Delta s = 0$ process which requires a particular type of admixing of A and B set wavefunctions. The valence band warping causes an admixing, but not of the proper form. However, both the linear-k and $k_3 \neq 0$ terms in the Hamiltonian do cause the desired type of admixing.

The linear-k case is particularly simple because it has been shown[24] that for magnetic fields above 30 kOe the main effect of the linear-k term is to cause an interaction between closely spaced A and B set heavy hole levels, i.e., the problem reduces to a series of two-level interactions. If one state of an admixed pair serves as an intermediate state for a $\Delta n = 1$, $\Delta s = 0$ process, the other state of the pair does also. The processes via this pair of states interfere and the combined cross section is $(\Delta E/E)^2$ times the cross section which would result if there were only a single intermediate state. ΔE is the energy separation between the interacting pair, and E is the intermediate minus initial energy. For the experimental conditions of Ref. 12, $\Delta E/E$ is about 3×10^{-3}, and the interference makes the cross section about 10^4 smaller than observed experimentally.

The $k_3 \neq 0$ induced process is more complicated because more than two states admix. We have made a numerical evaluation of the cross section appropriate to the experimental conditions of Ref. 12 using the eigenvectors and eigenvalues of the magnetic Hamiltonian of Ref. 23, but with k_3 terms included. We find the cross section for this process to be 10^3 to 10^4 smaller than experimentally observed. The interference between processes using different intermediate states reduces the cross section by a factor of 10^3 to 10^4 times the cross section from a single intermediate state.

We have two objections to the expressions for the $k_3 \neq 0$ cross sections of Refs. 18 and 19 First, the valence band states which serve as intermediate states under the experimental conditions of Ref. 12 are those at the top of the valence band and these most strongly exhibit the "quantum" effects (resulting from the energy degeneracy of light and heavy mass valence bands at k = 0). The energies and wavefunctions of these levels cannot be accurately calculated unless the band edge degeneracy is taken into account This apparently has not been done in the previous theoretical treatments. Second, and more important, the analytic expressions presented in Refs. 18 and 19 agree with what we calculate and compute for individual paths before summing over all allowed paths; i.e., the interference is not taken into account.

S. H. Groves
G. B. Wright

REFERENCES

1. S. Mase, J. Phys. Soc. Japan 14, 584 (1959).
2. Solid State Research Report, Lincoln Laboratory, M.I.T. (1968:3), p. 41.
3. L.D. Landau, Sov. Phys.–JETP 3, 920 (1956).
4. H.E. Stanley, Phys. Rev. 176, 718 (1968).
5. T.H. Berlin and M. Kac, Phys. Rev. 86, 821 (1952).
6. G.A. Smolenskii, V.M. Yudin, P.P. Syrnikov, and A.B. Sherman, ZhETF Pis. Red [JETP Lett.] 3, 416 (1966). [Sov. Phys.–JETP Lett. 3, 271 (1966).]
7. M.W. Shafer, T.R. McGuire, B.E. Argyle, and G.J. Fan, J. Appl. Phys. 39, 568 (1968).
8. G.A. Smolensky, R.V. Pisarev, M.P. Petrov, V.V. Moskalev, I.G. Siny, and V.M. Judin, J. Appl. Phys. 39, 568 (1968).
9. G. Zanmarchi and P.F. Bongers, Solid State Commun. 6, 27 (1968).
10. A. Pinczuk and E. Burstein, Phys. Rev. Letters 21, 1073 (1968).
11. M. Cardona, K.L. Shaklee, and F.H. Pollak, Phys. Rev. 154, 696 (1967).
12. R.E. Slusher, C.K.N. Patel, and P.A. Fleury, Phys. Rev. Letters 18, 77 (1967).
13. C.K.N. Patel and R.E. Slusher, Phys. Rev. 167, 413 (1968).
14. _____, Bull. Am. Phys. Soc. 13, 480 (1968).
15. P.A. Wolff, Phys. Rev. Letters 16, 225 (1966).
16. P.L. Kelley and G.B. Wright, Bull. Am. Phys. Soc. 11, 812 (1966).
17. Y. Yafet, Phys. Rev. 152, 858 (1966).
18. C.K.N. Patel, Proceedings of Symposium on Modern Optics, Vol. 17 (Polytechnic Press, Polytechnic Institute of Brooklyn, New York, 1967), p. 19.
19. V.P. Makarov, Sov. Phys.–JETP 55, 704 (1968).
20. G.B. Wright, P.L. Kelley, and S.H. Groves, Light Scattering in Solids, edited by G.B. Wright (Springer-Verlag, New York), Paper D-7 (to be published in 1969).
21. S.H. Groves and G.B. Wright (to be published).
22. J.M. Luttinger, Phys. Rev. 102, 1030 (1956).
23. C.R. Pidgeon and R.N. Brown, Phys. Rev. 146, 575 (1966).
24. C.R. Pidgeon and S.H. Groves, Phys. Rev. Letters 20, 1003 (1968), DDC 670787.

DOCUMENT CONTROL DATA – R&D

(Security classification of title, body of abstract and indexing annotation must be entered when the overall report is classified)

1. ORIGINATING ACTIVITY *(Corporate author)* Lincoln Laboratory, M.I.T.	2a. REPORT SECURITY CLASSIFICATION Unclassified 2b. GROUP None

3. REPORT TITLE

Solid State Research

4. DESCRIPTIVE NOTES *(Type of report and inclusive dates)*

Quarterly Technical Summary – 1 August through 31 October 1968

5. AUTHOR(S) *(Last name, first name, initial)*

McWhorter, Alan L.

6. REPORT DATE	7a. TOTAL NO. OF PAGES	7b. NO. OF REFS
15 November 1968	64	84

8a. CONTRACT OR GRANT NO. AF 19(628)-5167 b. PROJECT NO. 649L c. d.	9a. ORIGINATOR'S REPORT NUMBER(S) Solid State Research (1968:4) 9b. OTHER REPORT NO(S) *(Any other numbers that may be assigned this report)* ESD-TR-68-353

10. AVAILABILITY/LIMITATION NOTICES

This document has been approved for public release and sale; its distribution is unlimited.

11. SUPPLEMENTARY NOTES	12. SPONSORING MILITARY ACTIVITY
None	Air Force Systems Command, USAF

13. ABSTRACT

This report covers in detail the solid state research work at Lincoln Laboratory for the period 1 August through 31 October 1968. The topics covered are Solid State Device Research, Optical Techniques and Devices, Materials Research, and Physics of Solids.

14. KEY WORDS

solid state devices
optical techniques and devices
materials research
electron band structure
magnetism
laser research
infrared
photovoltaic detectors
crystal growth
magnetoreflection
rare-earth compounds
magneto-optical research
magnetoabsorption
laser scattering
Raman scattering